NASA-UVA LIGHT AEROSPACE ALLOY AND STRUCTURES TECHNOLOGY PROGRAM

LA^{2}ST

Supplement: RESEARCH ON MATERIALS FOR THE HIGH SPEED CIVIL TRANSPORT

Program Directors:

Edgar A. Starke, Jr.
Richard P. Gangloff

Co-principal Investigators:

Robert G. Kelly
John R. Scully
Glenn E. Stoner
John A. Wert

NASA-LaRC Grant Monitor:

Dennis L. Dicus

SEAS Report No. UVA/528266/MSE97/124
July 1997

Copy No.____

TABLE OF CONTENTS

NASA-UVa LIGHT AEROSPACE ALLOY AND STRUCTURES TECHNOLOGY PROGRAM *(LA²ST)*
Supplement: RESEARCH ON MATERIALS FOR THE HIGH SPEED CIVIL TRANSPORT

EXECUTIVE SUMMARY

This report documents the progress achieved over the period from January 1 to June 30, 1997 on three graduate student projects conducted within the NASA-UVa Light Aerospace Alloy and Structures Technology Program. These studies were aimed specifically at light metallic alloy issue relevant to the High Speed Civil Transport. The accomplishments presented in this report are summarized as follows.

Research on internal hydrogen embrittlement of high strength beta-titanium alloys establishes improved procedures for both introducing low levels of hydrogen, electrochemically, and measuring the initiation and growth fracture resistances of sheet. Experiments with solution treated and aged LCB sheet show that between 600 and 1000 wppm of predissolved hydrogen reduces the initiation toughness by up to 80%, substantially lowers the resistance of this alloy to stable crack growth, increases crack growth rate, and affects a fracture-mode transition. Hydrogen embrittlement is transgranular. Potentially hydrogen-resistant Ti-15-3 sheet has been obtained and is being prepared for similar studies. (Project #1)

Widely scattered fatigue initiation results prompted the suspension of fatigue testing on the Ti 15-3 open-hole M(T) specimen. Fatigue crack growth rate (FCGR) measurement of Ti 15-3 specimens heat treated in a furnace modified to improve lot to lot consistency is beginning. Fractured tensile and FCGR specimens will then be examined using electron microscopy to determine the nature of deformation involved in the fractures. (Project #2)

Creep behavior of candidate alloys reflects microstructural and compositional influence, being enhanced by the presence of the Ω phase and deteriorating with precipitation of the S' phase at grain boundaries and dislocations within the Al-Cu-Mg-Ag system. Creep exposure and elevated temperature microhardness testing of all alloys are continuing in order to provide valuable time-temperature-transformation (TTT) data

and to determine whether accelerated creep testing is possible for these alloys. (Project #3)

INTRODUCTION

Since 1986, the NASA-Langley Research Center has sponsored the NASA-UVa Light Alloy and Structures Technology (LA^2ST) Program at the University of Virginia (UVa). The fundamental objective of the LA^2ST program is to conduct interdisciplinary graduate student research on the performance of next generation, light-weight aerospace alloys, composites and thermal gradient structures. The LA^2ST program has aimed to product relevant data and basic understanding of material mechanical response, environmental/corrosion behavior, and microstructure; new monolithic and composite alloys; advanced processing methods; measurement and modeling advances; and a pool of educated graduate students for aerospace technologies. The scope of the LA^2ST Program is broad. Research areas include: (1) Mechanical and Environmental Degradation Mechanisms in Advanced Light Metals and Composites, (2) Aerospace Materials Science, (3) Mechanics of materials for Aerospace Structures, and (4) Thermal Gradient Structures. A substantial series of semi-annual progress reports issued since 1987 documents the technical objectives, experimental or analytical procedures, and detailed results of graduate student research in these topical areas.

As documented in the most recent progress report,[1] LA^2ST productivity since 1986 includes: 130 publications (86 archival journal or reviewed book publications), 26 PhD dissertations or MS theses, 129 external technical presentations, 22 NASA progress reports and 5 NASA Contractor Reports. Since 1986, 37 graduate students, including 34 citizens of the United States, have been involved with LA^2ST research; 28 have received the MS or PhD degree. Seven post-doctoral research associates have participated in LA^2ST research, along with a total of 13 faculty.

In October of 1991, E.A. Starke proposed a substantial supplement to the base LA2ST Program. The objective of this research was to involve UVa faculty with engineering scientists from aluminum alloy producers and airframe manufacturers in a broad research program to develop light aluminum alloys and composites for elevated

[1] R.P. Gangloff and E.A. Starke, Jr., *NASA-UVA Light Aerospace Alloy and Structures Technology Program*, Report No. UVA/528266/MS97/123, University of Virginia, Charlottesville, VA, February, 1997.

temperature-long time High Speed Civil Transport (HSCT) applications.[2,3] NASA-Langley Research Center (LaRC), ALCOA, Allied-Signal, Boeing, McDonnell Douglas, Reynolds Metals and UVa joined in an effort to identify the most promising aluminum-based materials with respect to major structural use on the HSCT and to further develop those materials. This research began in January of 1992 and results were reported separately from the LA^{2}ST program.[4] In 1994 HSCT research at UVa was expanded to include titanium alloys, and collaborations were implemented with RMI Titanium Company and TIMET. These titanium projects were reported in base LA^{2}ST progress reports, as was aluminum HSCT work performed during 1995 and beyond. In mid-1996, NASA requested that those LA^{2}ST dealing with HSCT materials issues be reported separately.[5]

Three HSCT research projects were conducted at UVa in 1996, involving two PhD graduate students, Sean P. Hayes (advised by Professor Gangloff) and Susan M. Kazanjian (advised by Professor Starke), as well as a Post-doctoral Research Associate supervised by E.A. Starke. Research progress, recorded during the period from January 1, 1997 to June 30, 1997, is summarized in the following three sections. Each section contains a problem statement, research objective, approach, recent results, conclusions, and future milestones. These discussions are coupled with copies of viewgraphs presented at the Eighth Annual NASA-UVa LA^{2}ST Grant Review Meeting held at the Langley Research Center in July of 1997.

---

[2] R.P. Gangloff, E.A. Starke, J.M. Howe and F.E. Wawner, *NASA-UVa Light Aerospace Alloy and Structures Technology Program: Supplement on Aluminum Based Materials for High Speed Aircraft*, Proposal No. MS NASA/LaRC-5215-92, University of Virginia, 1991.

[3] R.P. Gangloff, E.A. Starke, J.M. Howe and F.E. Wawner, *NASA-UVa Light Aerospace Alloy and Structures Technology Program: Supplement on Aluminum Based Materials for High Speed Aircraft*, Proposal No. MS NASA/LaRC-5691-93, University of Virginia, 1992.

[4] E.A. Starke, Jr., *NASA-UVa Light Aerospace Alloy and Structures Technology Program: Supplement on Aluminum Based Materials for High Speed Aircraft*, NASA Contractor Report 4517, June, 1993.

[5] R.P. Gangloff and E.A. Starke, Jr., *NASA-UVa Light Aerospace Alloy and Structures Technology Program: Supplement on Aluminum Based Materials for High Speed Aircraft*, Report No. UVA/528266/MSE97/122, March, 1997.

RESEARCH RESULTS

Project #1: Mechanisms of Deformation and Fracture in High-Strength Titanium Alloys: Effect of Dissolved Hydrogen

Sean P. Hayes and R.P. Gangloff

Problem Statement

Metastable β-titanium alloys are candidates for the airframe of the High Speed Transport (HSCT). Two metastable β-titanium alloys in sheet form are being investigated for this application; Low Cost Beta and Ti-15-3. Potential problems and uncertainties are associated with the complex nature of the fracture processes in titanium alloys and with the potential for long-term alloy degradation due to hydrogen embrittlement.

Objectives

The broad objective of this research is to define the hydrogen concentrations and microstructural conditions that promote internal hydrogen embrittlement in two solution treated and aged (STA), high strength, β-titanium alloys; Low Cost Beta and Ti-15-3, in sheet form. The objectives of this reporting period include (1) characterizing the initiation fracture toughness and K vs Δa resistance curves of STA LCB sheet at 23°C, (2) determining the hydrogen concentration dependence of both the threshold stress intensity and subcritical crack growth rates of STA LCB sheet, (3) determining the microscopic processes involved in ductile fracture and hydrogen embrittlement, and (4) initiating similar work on Ti-15-3.

Current Status

The current work in this project has focused on hydrogen-precharging and room temperature fracture toughness testing of STA LCB and Ti-15-3 sheet in both the as-received and hydrogen-precharged conditions. Previous hydrogen charging results demonstrate that hydrogen uptake is prevented at current densities less than

approximately 0.2 mA/cm^2. This is problematic in that when the calibration relationship is extrapolated from the high current density-high hydrogen concentration range to the desired-low hydrogen concentration levels, the corresponding current densities are insufficient to destabilize the surface oxide, and hydrogen uptake is blocked. This problem has been circumvented by charging at higher current densities for shorter times, followed by furnace heating to allow for hydrogen homogenization through the specimen thickness. This approach improved the calibration relationship significantly, reduced hydrogen concentration variability in LCB, and was successfully applied to STA Ti-15-3 sheet.

The rising CMOD R-curve test methodology, which utilizes direct current potential difference (dcPD) to detect crack growth initiation and monitor crack growth, has been improved by increasing the bit-resolution of the analog to digital processor, programming new software for data acquisition, electrically isolating the specimen, and implementing a reference probe. Interrupted rising CMOD tests show that this improved test method detects highly localized crack tip process zone damage. These interrupted tests confirm that the apparently low reported values of crack growth initiation fracture toughness for STA LCB are accurate and reproducible. The reduced toughnesses are a result of the increased sensitivity of detecting crack growth initiation, coupled with the inherently low fracture toughness of high strength β/α-titanium alloys.

Current research is focused on more precisely determining the threshold hydrogen concentration necessary to trigger severe embrittlement of STA LCB sheet at room temperature and a fixed, slow loading rate. Rising CMOD R-curve test results demonstrate that moderate hydrogen concentrations (~300 wppm) reduce initiation fracture toughness by 25 percent, while intermediate concentrations (~ 500 wppm) reduce initiation fracture toughness by 50 percent. Significant embrittlement is triggered at approximately 750 wppm H, as demonstrated by a reduction in initiation fracture toughness by 80 percent.

Ti-15-3 sheet was obtained and heat treated. Initial hydrogen charging experiments were successful.

Recent Results

The calibration curves relating the applied cathodic current density, time, and hydrogen uptake in STA LCB sheet exposed to aqueous H_2SO_4 + $Na_4P_2O_7$ at 90°C were improved significantly. Short-term high current density charging and air homogenization at 90°C effectively introduce low levels of hydrogen into STA LCB and Ti-15-3 sheet. The rate of hydrogen uptake for Ti-15-3 is nearly three times greater than for LCB at a constant current density of 1.5 mA/cm^2 and variable charging times.

The rising CMOD, R-curve results establish that the room temperature fracture toughness of STA LCB sheet is relatively low without hydrogen precharging. The average plane strain initiation fracture toughnesses, K_{JCi} and K_{JC}, for as-received STA LCB sheet are 38.2 and 58.2 MPa$\sqrt{m}$, respectively. The initiation fracture toughness values from the improved acquisition system are consistently lower than previously reported values. Interrupted rising CMOD R-curve tests confirm dcPD indications of crack growth; extensions of 100 and 175 μm occurred at stress intensities of 34.4 and 39.9 MPa$\sqrt{m}$, respectively, while no crack extension occurred at 27.5 MPa$\sqrt{m}$. Measured crack lengths from the interrupted tests agree reasonably with the R-curves from the replicate tests using the improved dcPD system.

The initiation fracture toughness of LCB sheet is reduced by modest concentrations of predissolved hydrogen and is significantly reduced near 1000 wppm H. Rising CMOD R-curve test results demonstrate that moderate hydrogen concentrations (~300 wppm) reduce initiation fracture toughness by 25 percent, while intermediate concentrations (~ 500 wppm) reduce initiation fracture toughness by 50 percent. Significant embrittlement is triggered at approximately 750 wppm H, with a reduction in initiation fracture toughness of 80 percent.

The increase in subcritical crack growth rates with increasing hydrogen concentration does not correspond directly with the reduction in initiation fracture toughness. Instead, there is a mild increase in crack growth rates with increasing hydrogen concentrations up to approximately 700 wppm. Crack growth rates increase sharply above this concentration as demonstrated by the two orders of magnitude increase

in da/dt for the specimen containing 1150 wppm H relative to as-received specimens (236 wppm H).

Fractography of CT specimens indicates that predissolved hydrogen causes a change in fracture mode which depends on hydrogen concentration. The fracture mechanisms in as-received CT specimens are complicated but show dimpled rupture features, while the CT specimen that was hydrogen precharged to 1150 wppm H failed by transgranular cleavage. Intermediate hydrogen concentrations failed by mixed fracture modes.

Future Work

Work over the next six months will focus on: (1) precisely determining the critical hydrogen concentration necessary for severe hydrogen embrittlement in STA LCB at room temperature and a fixed slow loading rate, (2) correlating microstructural features with fracture modes in LCB to understand the role of dissolved hydrogen on fracture, and (3) investigating the effect of predissolved hydrogen on fracture toughness and crack growth rates in STA Ti-15-3 sheet.

Presentation Captions

1. Title

2. Problem Statement

3. Plots showing the effect of hydrogen concentration on the maximum longitudinal stress and the average plastic strain to fracture for peak aged 15-3 and 21S circumferentially notched tensile specimens. These data show the deleterious effects of predissolved hydrogen in β-titanium alloys. Low C_H levels and sheet microstructures have not been investigated, and are the focus of current, more rigorous fracture mechanics experiments.

4. Objectives

5. Compositions and aging conditions of Timet LCB and Ti-15-3 sheet.

6. Backscattered electron images (BEI) of STA LCB sheet. These show beta grain boundaries, and the morphology and distribution of the alpha phase. The alpha particles are on the order of 1 μm in length and it appears that a continuous alpha phase exists along some beta grain boundaries.

7. Secondary electron images (SEI) of STA Ti-15-3 sheet. These show beta grain boundaries, and the morphology and distribution of the alpha phase. A classic basket-weave structure exists with relatively coarse alpha and colonies of alpha occasionally formed at prior beta grain boundaries.

8. Schematic diagram of the rising CMOD R-curve test setup showing CT specimen, buckling restraints, isolation grips, crack mouth opening displacement measurement by clip gage, reference probe, current leads, and dcPD probes. This apparatus is used to determine fracture toughness of thin sheet alloys.

9. Plots showing the evolution of test data in developing an R-curve from a four-hour rising CMOD test. The cracked-sample raw dcPD signal decreased with increasing CMOD, which masked crack-growth initiation. Raw dcPD values exhibited other forms of variability, dictating the use of a reference probe. The load and true dcPD signal, adjusted using the reference probe, are plotted versus CMOD. The CMOD at dcPD-detected crack-growth initiation is labeled ($CMOD_i$). The K-Δa resistance curve is generated from these data, based on crack-growth initiation as determined by the true dcPD signal.

10. This equation is used to adjust the raw dcPD signal, where $V_{Ref,o}$ is the initial reference probe potential and V_{Ref} is the reference probe potential at any time, t. The as-received-alloy fracture toughness values, determined using the improved test methodology, are shown. Only dcPD-detected initiation fracture toughness values (K_{JICi}) are given for the interrupted tests because insufficient crack growth occurred to determine valid K_{JIC} values.

11. Interrupted test data plotted with as-received replicate R-curves verify that crack growth initiation in LCB sheet CT specimens occurs at stress intensities ranging from 33 to 40 MPa$\sqrt{m}$. The reference-probe corrected dcPD values provide a sensitive indication of the initiation of crack growth in high strength β/α Ti alloy sheet specimens.

12. Fracture surfaces showing the amount of stable crack extension from interrupted rising CMOD tests represented in Figures 10 and 11. The fracture surfaces were marked by fatigue after the rising CMOD tests were interrupted. This delineated the stable crack growth and allowed for multiple tests on one fracture mechanics specimen.

13. Fracture toughness versus ultimate tensile strength (UTS) for TIMET LCB sheet and other β-titanium alloys with various processing conditions. The toughness of LCB sheet is comparable to other β-titanium alloys investigated. The stress intensity range at which process zone damage initiates, as detected by dcPD, is labeled.

14. Calibration curve relating the applied cathodic current density and hydrogen uptake in STA LCB sheet exposed to aqueous H_2SO_4 + $Na_4P_2O_7$ at 90°C for 50 hours. These data show that hydrogen uptake is prevented at current densities less than approximately 0.2 mA/cm^2. Low current densities are insufficient to destabilize the surface oxide which prevents hydrogen uptake.

15. Calibration curves relating the applied cathodic current density, time, and hydrogen uptake in STA LCB sheet exposed to aqueous H_2SO_4 + $Na_4P_2O_7$ at 90°C. Short-term high current density charging and air homogenization at 90°C effectively introduce low levels of hydrogen.

16. Calibration curve relating the time and hydrogen uptake in STA Ti-15-3 sheet exposed to aqueous H_2SO_4 + $Na_4P_2O_7$ at 90°C and a fixed cathodic current density of 1.5 mA/cm^2. Short-term high current density charging and air homogenization at 90°C effectively introduce low levels of hydrogen. The rate of hydrogen uptake for Ti-15-3 is nearly three times greater than that for LCB.

17. Stress intensity versus crack extension R-curves for STA LCB sheet CT specimens in the as-received and hydrogen precharged conditions at room temperature and constant rising-displacement rate conditions. The reduction in the R-curve with increasing precharged hydrogen concentration is apparent.

18. Rising CMOD R-curve test results clearly demonstrate the reduction in initiation fracture toughness, with mildly increasing hydrogen concentration, for precharged STA LCB sheet fractured by slow loading at 23°C.

19. Results reported by Scully and coworkers establish the reduction in initiation fracture toughness, with increasing hydrogen concentration, for precharged STA Beta 21S and Ti-15-3 fractured by slow loading at 23°C. The results for precharged LCB suggest that the deleterious effect of dissolved hydrogen occurs at lower concentrations compared to other β-titanium alloys investigated.

20. Crack growth rate versus predissolved hydrogen concentration for LCB sheet CT specimens tested under identical temperature and rising-displacement rate conditions. Subcritical crack growth rates increase mildly with increasing C_H levels to approximately 700 wppm. The crack growth rate rises sharply at this concentration.

21. Fractography of LCB sheet CT specimens containing 236 (A.R), 280, and 310 wppm H with their initiation fracture toughness values. These fracture surfaces demonstrate that the fracture modes in CT specimens with as-received C_H levels are complicated but show dimpled rupture features. Mild increases in C_H levels reduce fracture toughness values and alter fracture modes.

22. Fractography of LCB sheet CT specimens containing 490*, 535*, 770, and 1150 wppm H with their initiation fracture toughness values. The intermediate C_H-level fracture surfaces contain features similar to the as-received condition, but a significant change in fracture mode with increasing C_H levels is apparent. The specimen with 1150 wppm H failed primarily by transgranular cleavage, while intermediate C_H levels fail by mixed modes. This behavior is significantly different from other β-titanium alloys in which intergranular cracking is observed at intermediate C_H levels.

23. Room temperature fracture toughness and hydrogen embrittlement results for TIMET LCB CT specimens. The subscript i denotes that crack initiation was detected using the dcPD system. A 0.2 mm offset blunting line, as defined in ASTM E 813, was used to determine J_{IC} and K_{JIC} values.

24. Conclusions

25. Future Work

Mechanisms of Deformation and Fracture in High Strength Titanium Alloys: Effect of Dissolved Hydrogen

Sean P. Hayes and Richard P. Gangloff

Funded by NASA Langley Research Center
Dennis Dicus, Grant Monitor
July 24, 1997

Problem:

Engineering

- Characterizing high strength β-titanium alloys for HSCT applications, with regards to low C_H and sheet microstructural features that promote hydrogen embrittlement

Science

- Understanding how and why hydrogen damage occurs

Longitudinal Stress vs. Hydrogen Concentration

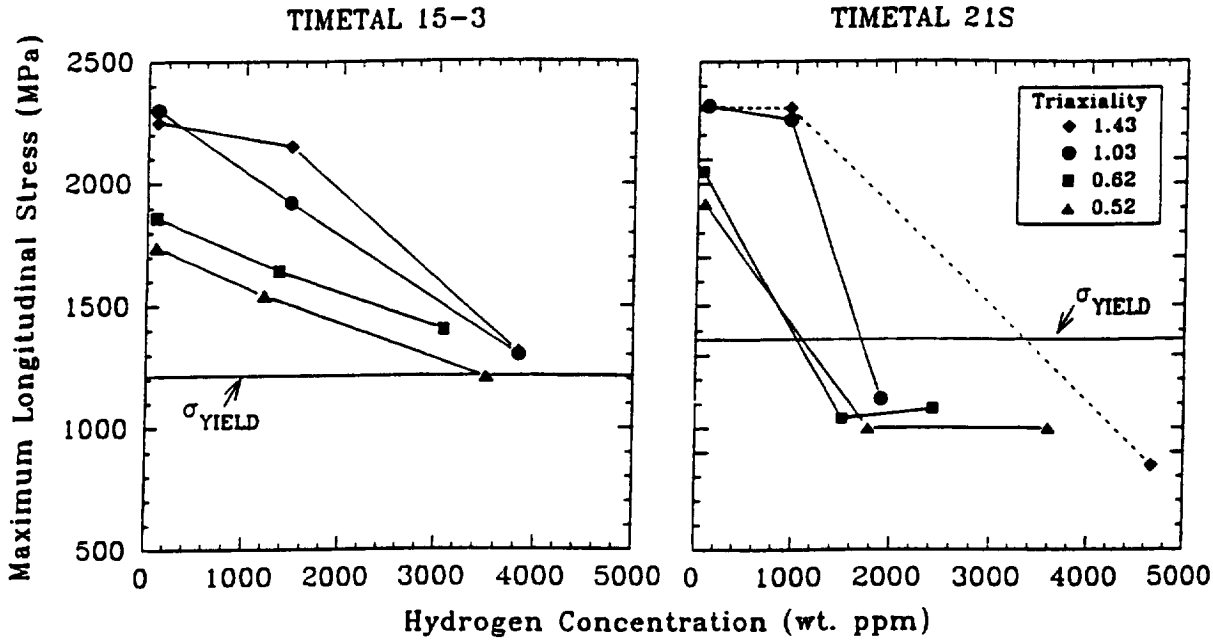

Plastic Strain vs. Hydrogen Concentration

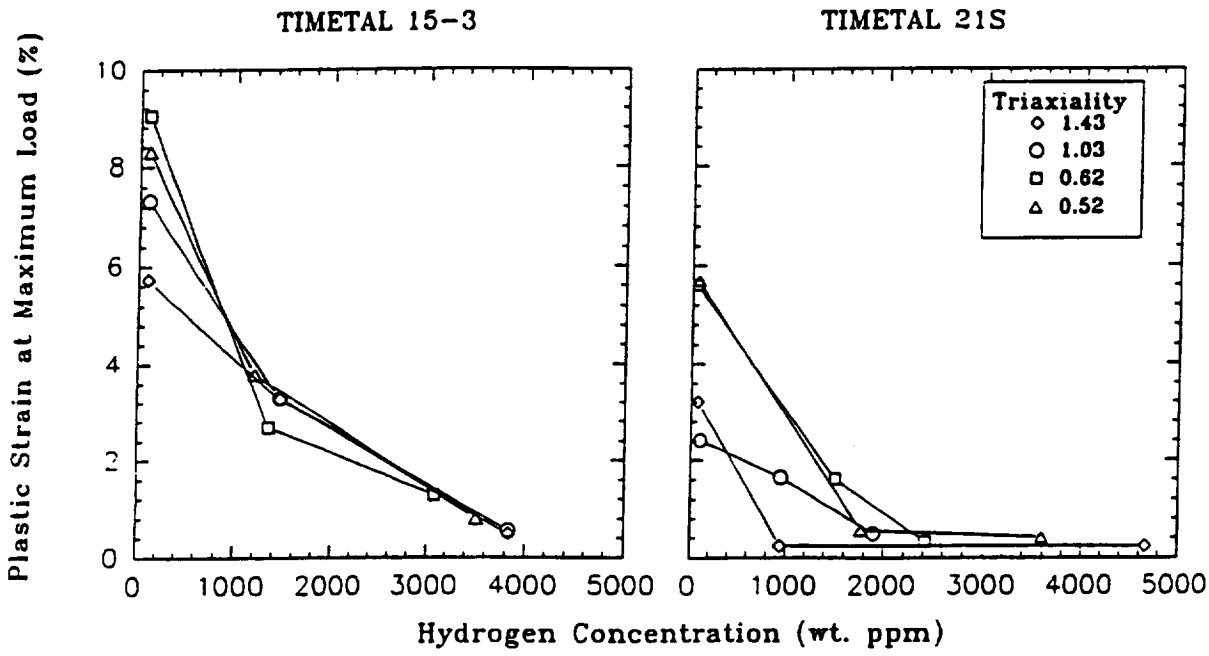

Generated from circumferentially notched tensile specimens
G. A. Young and J. R. Scully

Objectives

Characterize and understand effects of predissolved hydrogen on fracture resistance of solution treated and aged β/α-Ti alloy sheet microstructures.

- Develop method and characterize the initiation fracture toughness and K vs Δa resistance behavior of STA LCB.
- Develop a procedure to precisely control predissolved C_H levels.
- Determine the C_H dependence of threshold stress intensity and subcritical crack growth rates for LCB.
- Characterize the microscopic processes involved in ductile fracture and hydrogen embrittlement.
- Initiate similar work on Ti-15-3.

LCB Composition (wt. pct.)

Ti	Mo	Fe	Al	O	H
Bal.	6.8	4.5	1.5	0.09	0.0236

LCB Sheet

β Transus ~ 790°C

α/β S.T. 760°C - 20 minutes

Aged 593°C - 20 hrs

β Grain Size ~ 20-100 μm

HRC ~ 40 ➜ UTS ~ 1200 MPa

Ti-15-3 Composition (wt. pct.)

Ti	V	Al	Cr	Sn	Fe	Si	C	O	N	H
Bal.	15.0	3.0	3.0	3.0	0.17	0.06	0.01	0.11	0.017	0.0031

Ti-15-3 Sheet

β Transus ~ 770°C

β Solution Treated

Aged 510°C - 12 hrs

β Grain Size = 32 μm

HRC ~ 38 ➜ UTS ~ 1150 MPa

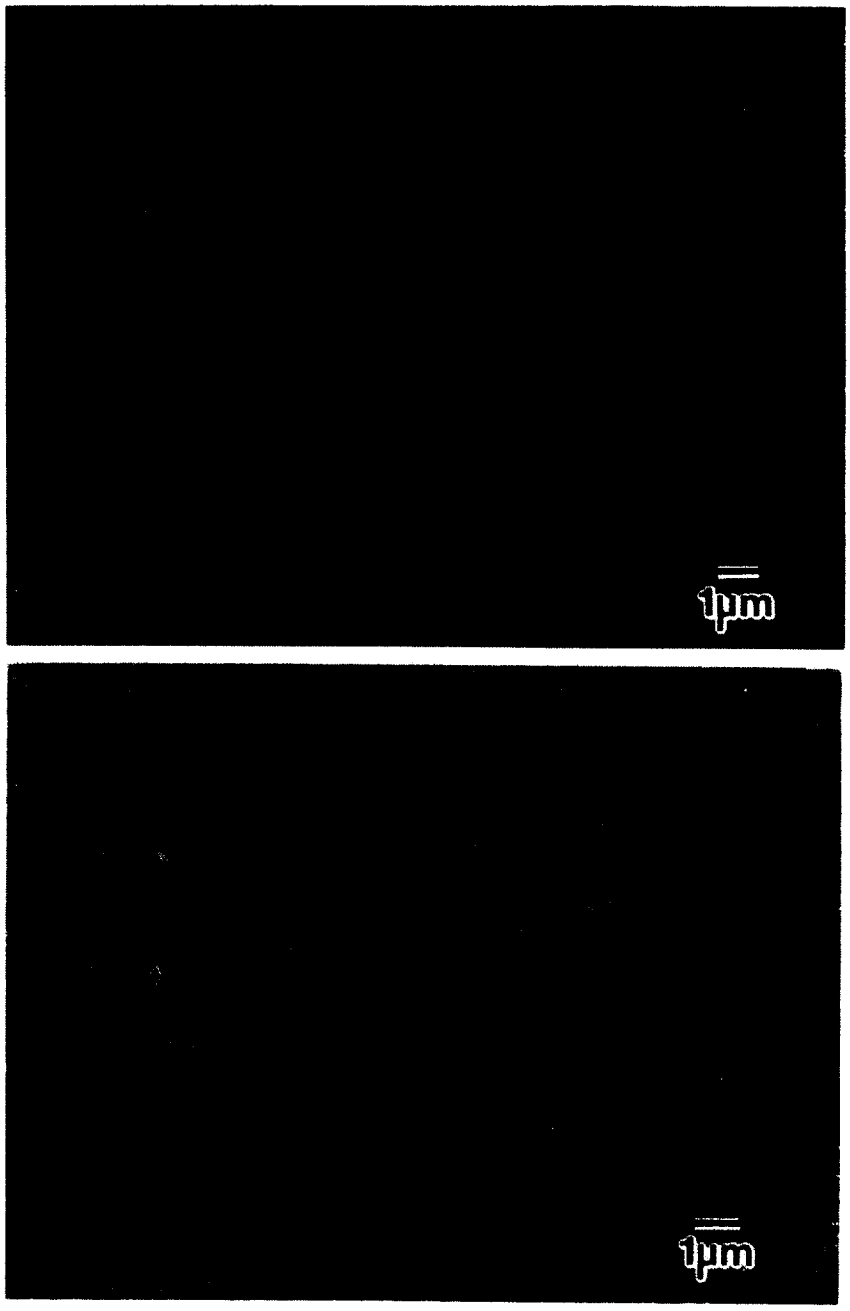

LCB BEI

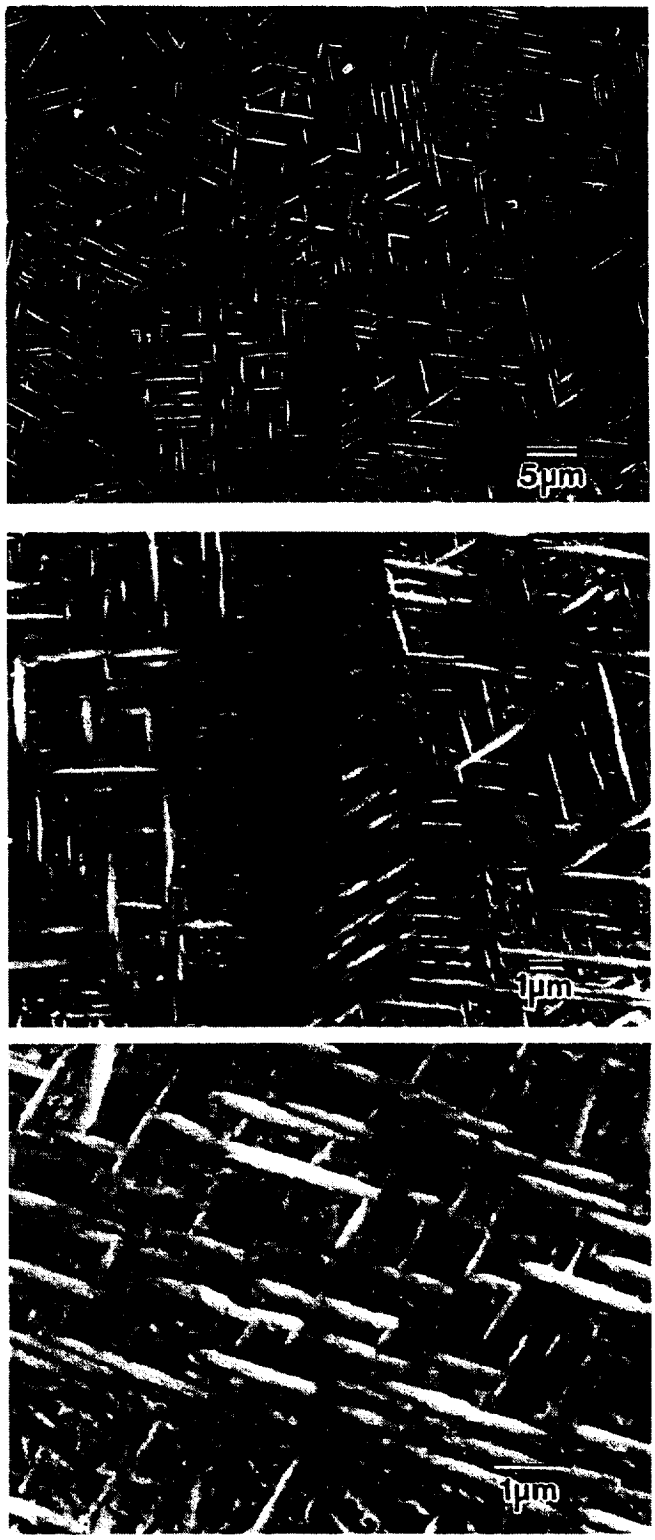

Ti-15-3 SEI

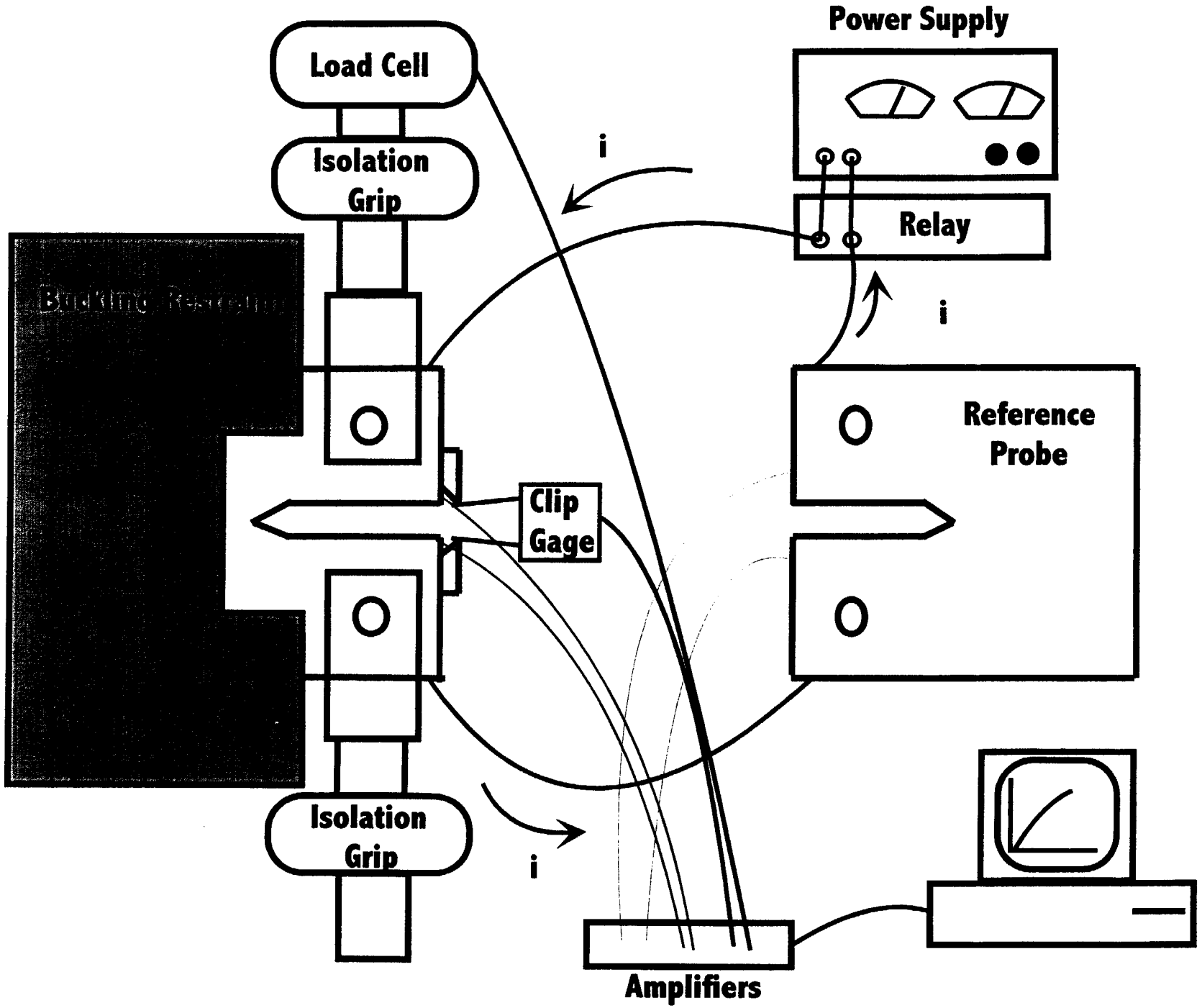
Power Supply
Load Cell
Isolation Grip
i
Relay
i
Reference Probe
Clip Gage
Isolation Grip
i
Amplifiers

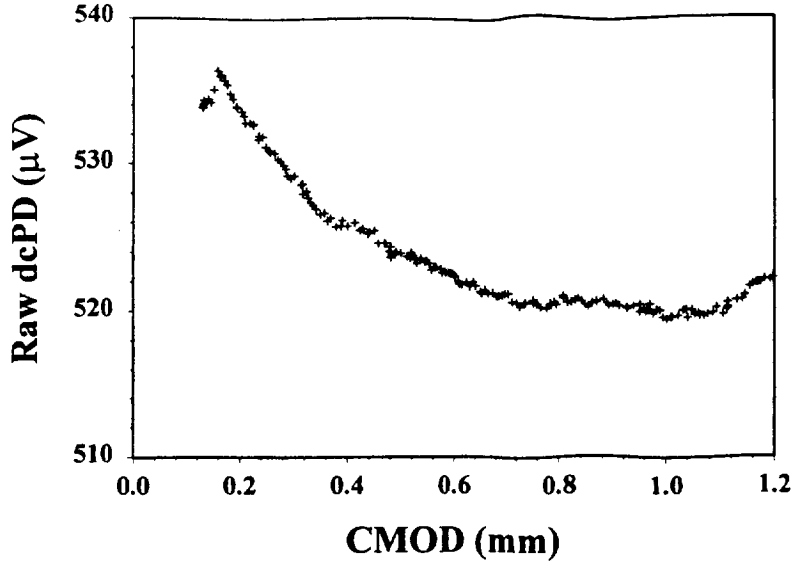

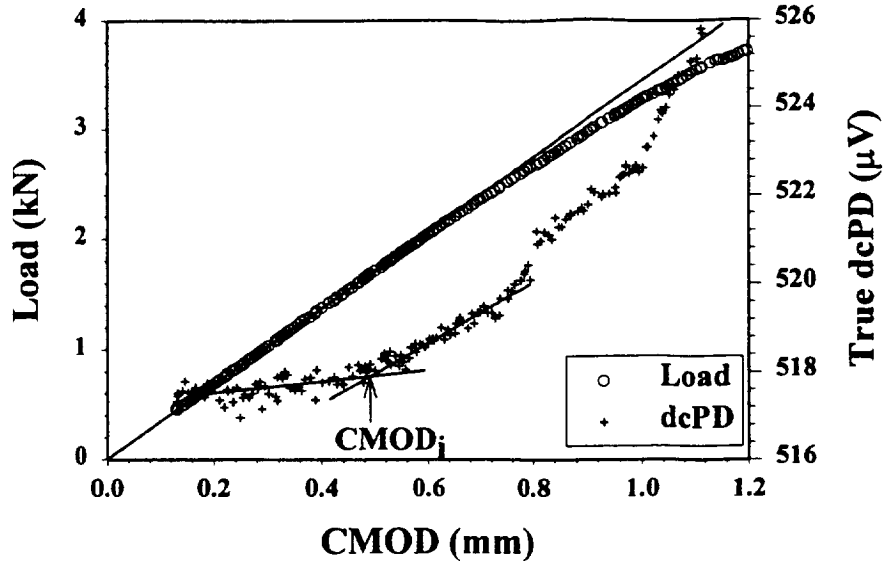

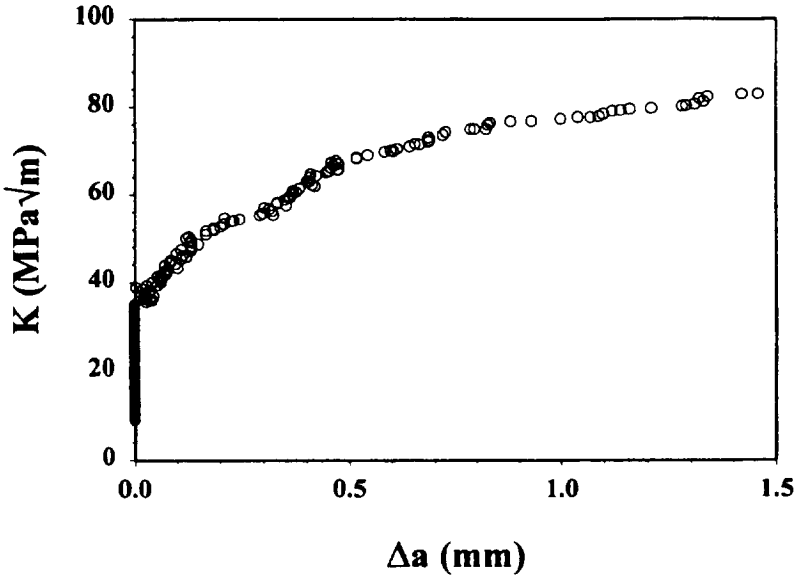

STA LCB
1.7 mm sheet
dδ/dt = 5.08 μm/sec
23°C

$$V_{True} = V_{Raw}\left(\frac{V_{Ref,o}}{V_{Ref}}\right)$$

where each dcPD is corrected for Thermal emf.

Specimen I.D.	K_{JICi} (MPa$\sqrt{m}$)	K_{JIC} (MPa$\sqrt{m}$)
Sheet 16	40.6	64.0
Sheet 17	34.9	54.0
Sheet 18	39.1	56.7
Sheet 18 (Interrupted)	33.4 33.9 35.2	-- -- --

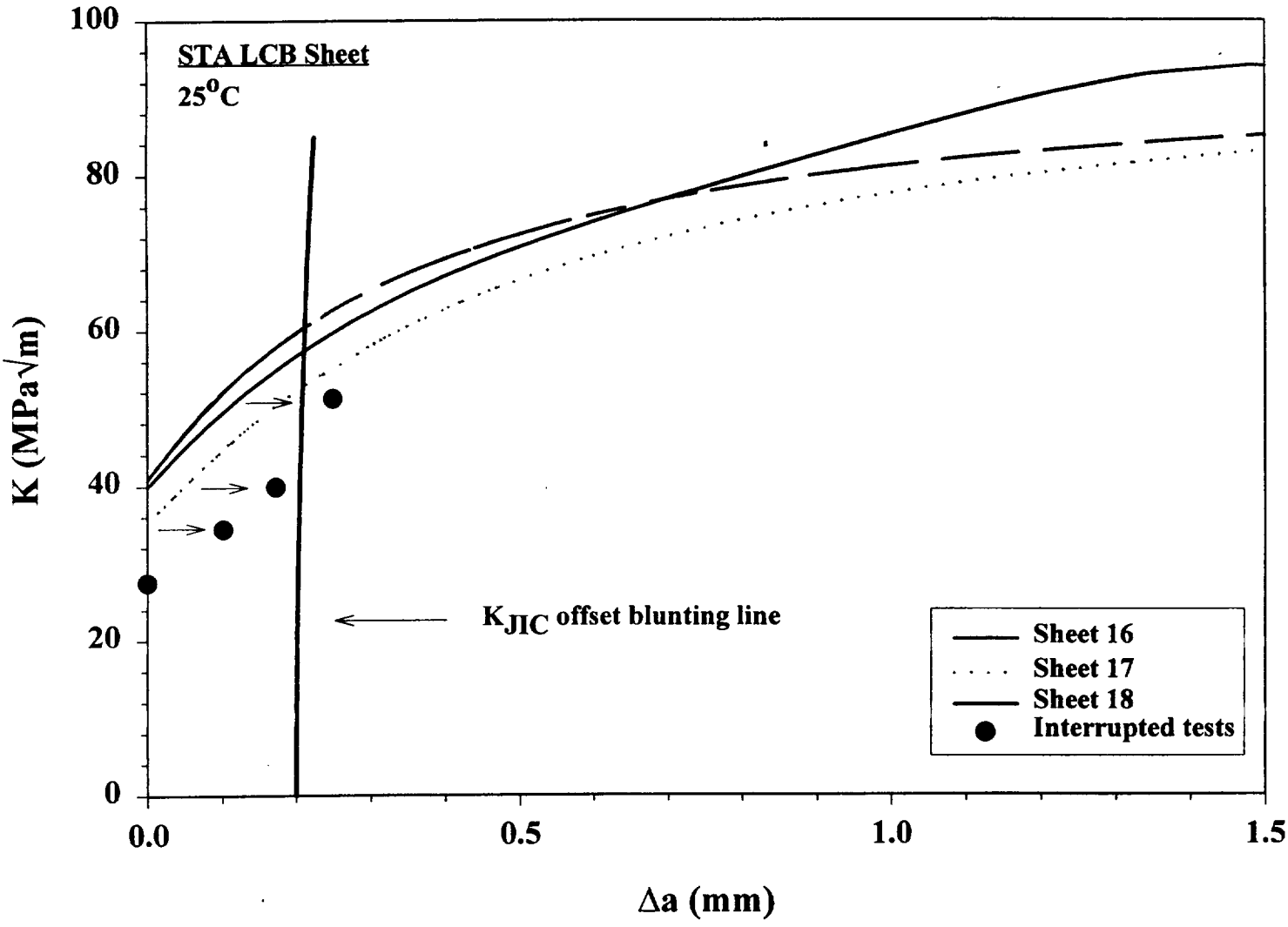
STA LCB Sheet
25°C
100
80
60
40
20
0
K (MPa√m)
0.0
0.5
1.0
1.5
Δa (mm)
K_JIC offset blunting line
Sheet 16
Sheet 17
Sheet 18
Interrupted tests

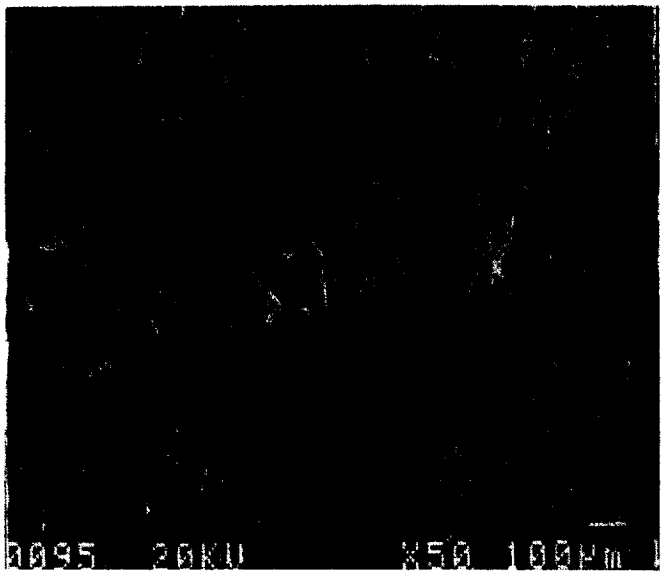

K = 27.5 MPa√m
Measured Δa = 0 µm

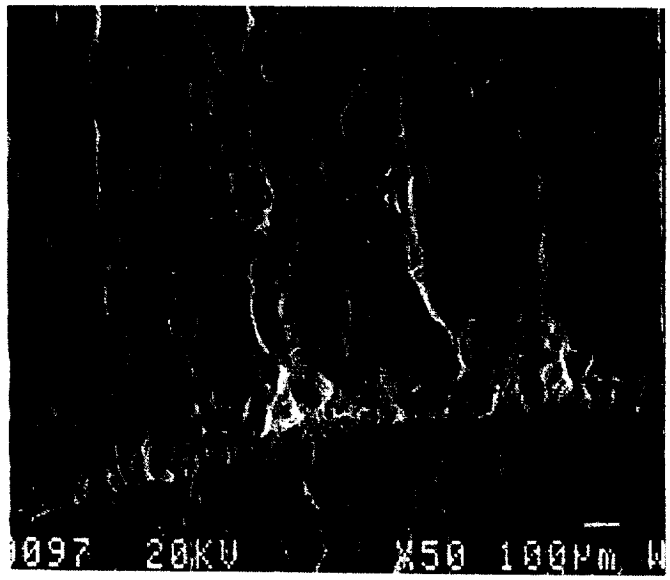

K = 34.4 MPa√m
Measured Δa = 102 µm

K = 39.9 MPa√m
Measured Δa = 173 µm

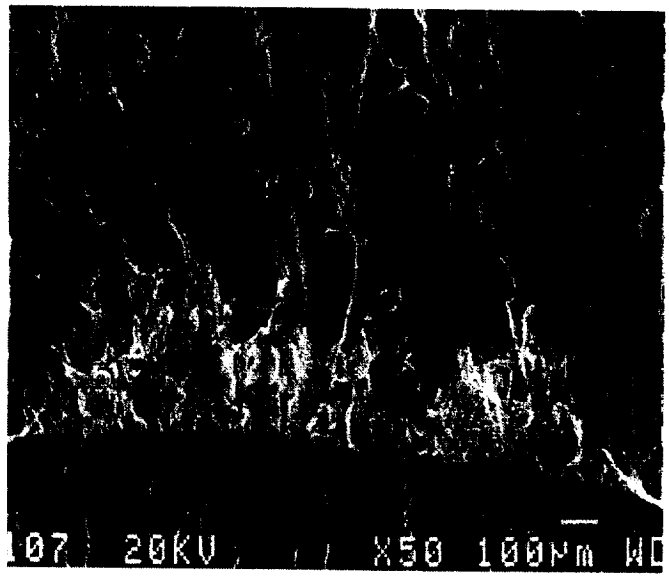

K = 51.2 MPa√m
Measured Δa = 250 µm

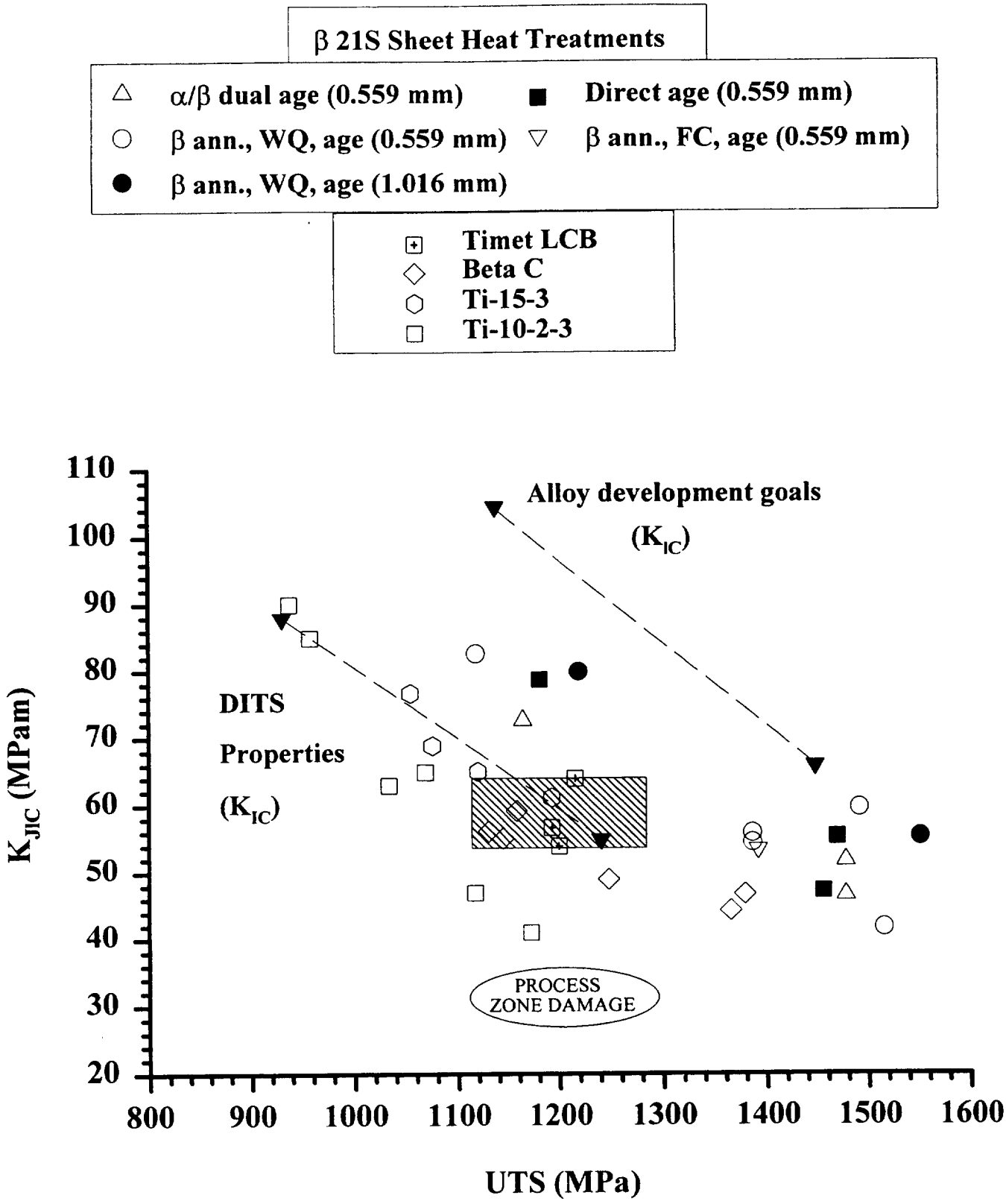
β 21S Sheet Heat Treatments
α/β dual age (0.559 mm)
Direct age (0.559 mm)
β ann., WQ, age (0.559 mm)
β ann., FC, age (0.559 mm)
β ann., WQ, age (1.016 mm)
Timet LCB
Beta C
Ti-15-3
Ti-10-2-3
Alloy development goals
(K_{IC})
DITS
Properties
(K_{IC})
PROCESS
ZONE DAMAGE
K_{JIC} (MPam)
UTS (MPa)
110
100
90
80
70
60
50
40
30
20
800
900
1000
1100
1200
1300
1400
1500
1600

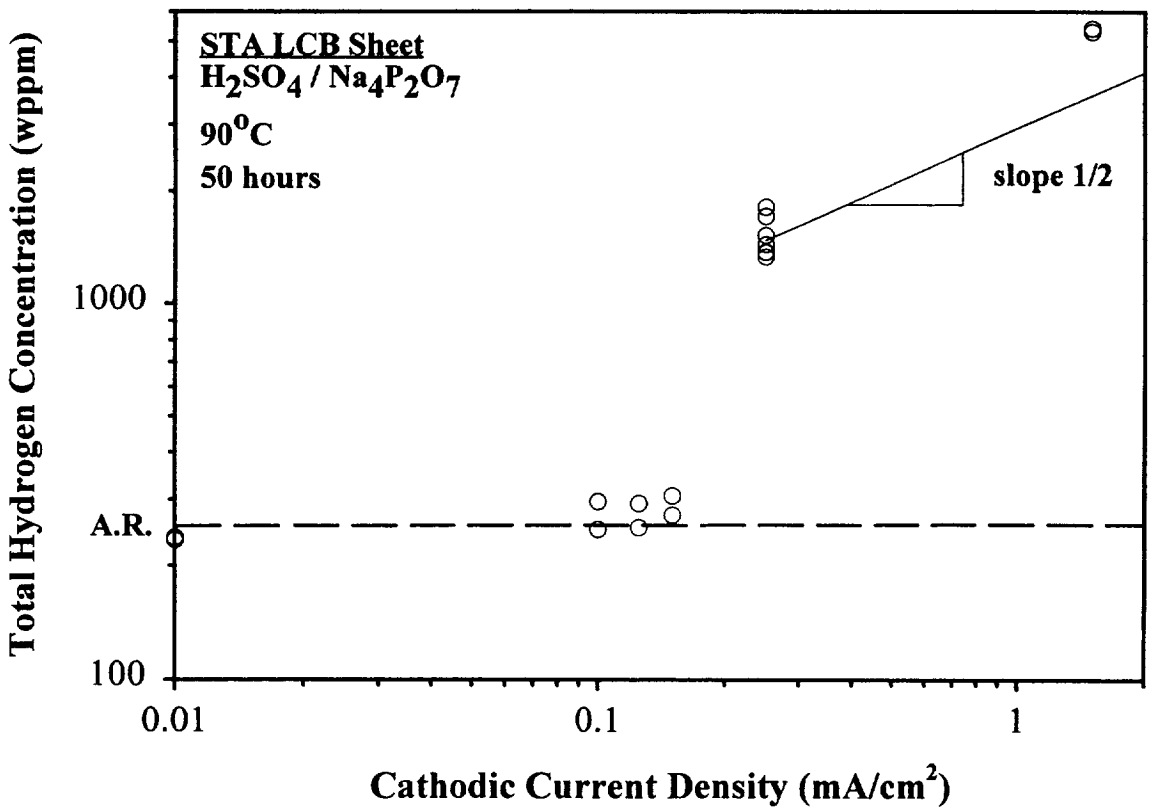
STA LCB Sheet
H_2SO_4 / $Na_4P_2O_7$
90°C
50 hours
slope 1/2
1000
A.R.
100
0.01
0.1
1
Total Hydrogen Concentration (wppm)
Cathodic Current Density (mA/cm²)

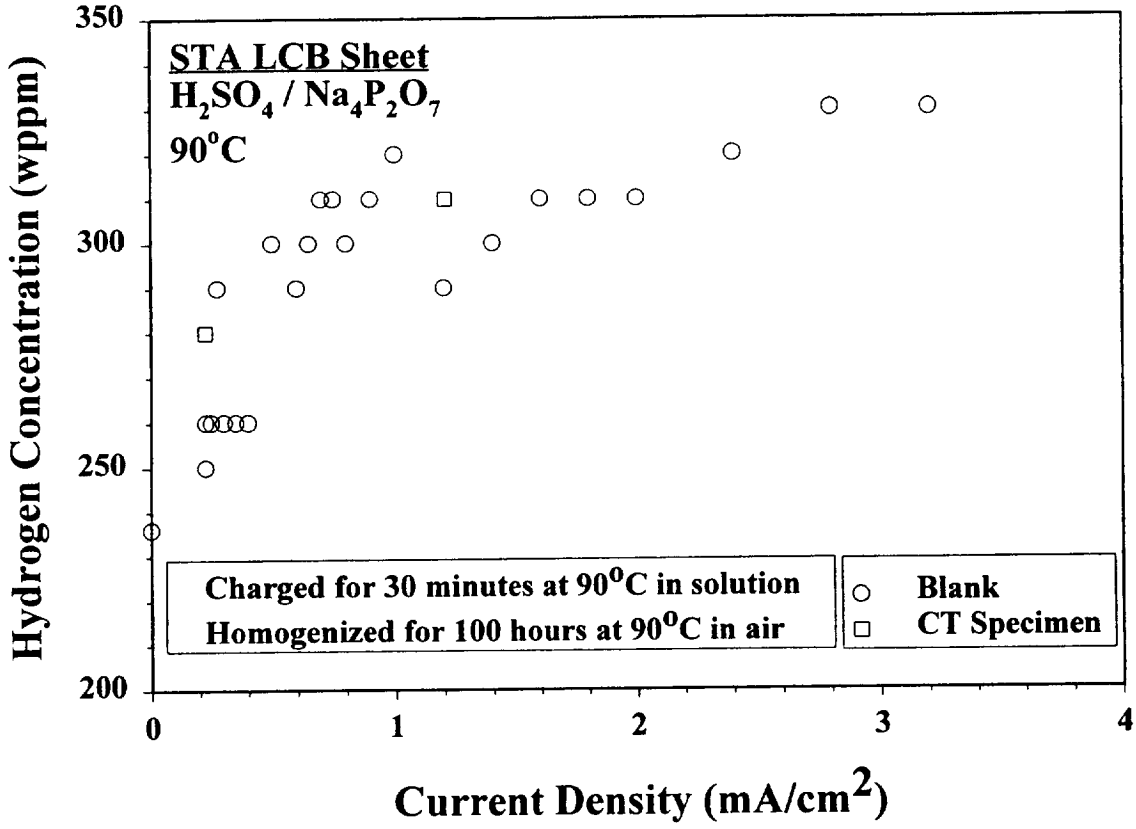
STA LCB Sheet
H_2SO_4 / $Na_4P_2O_7$
90°C
Charged for 30 minutes at 90°C in solution
Homogenized for 100 hours at 90°C in air
Blank
CT Specimen
Hydrogen Concentration (wppm)
Current Density (mA/cm²)
350
300
250
200
0
1
2
3
4

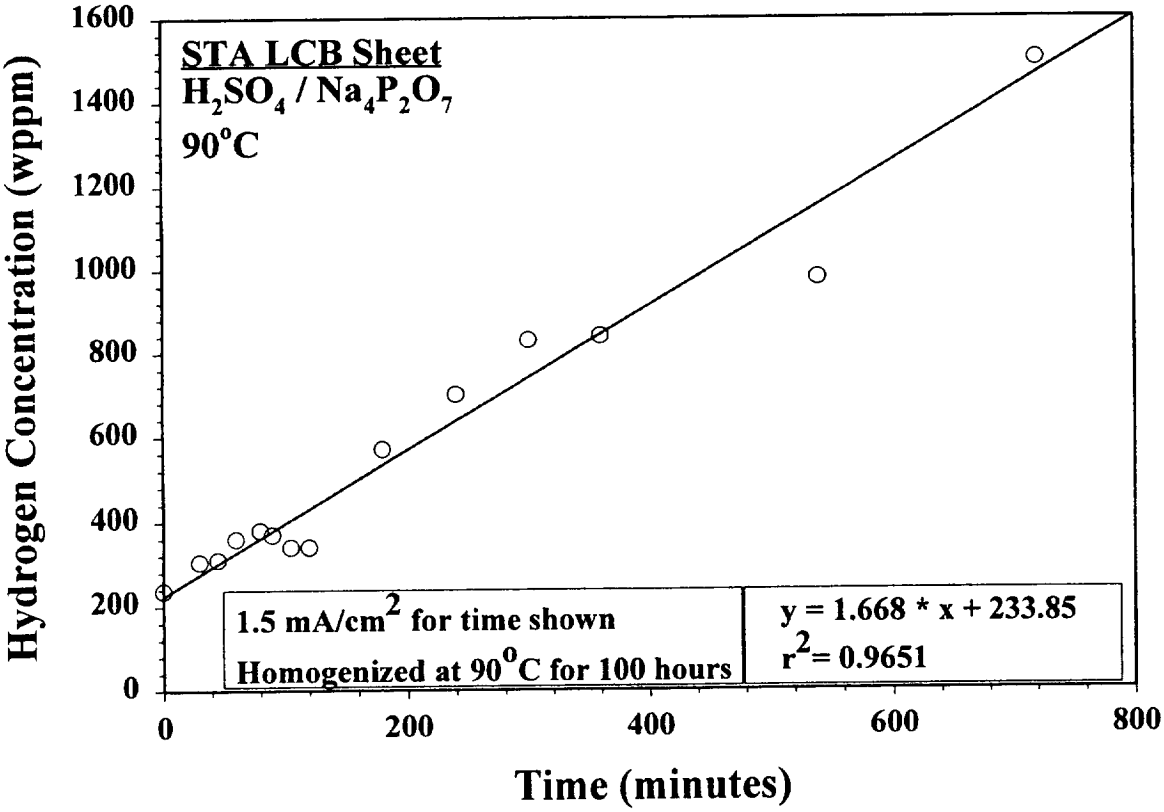
STA LCB Sheet
H_2SO_4 / $Na_4P_2O_7$
90°C
1.5 mA/cm² for time shown
Homogenized at 90°C for 100 hours
y = 1.668 * x + 233.85
r² = 0.9651
Hydrogen Concentration (wppm)
Time (minutes)
1600
1400
1200
1000
800
600
400
200
0
0
200
400
600
800

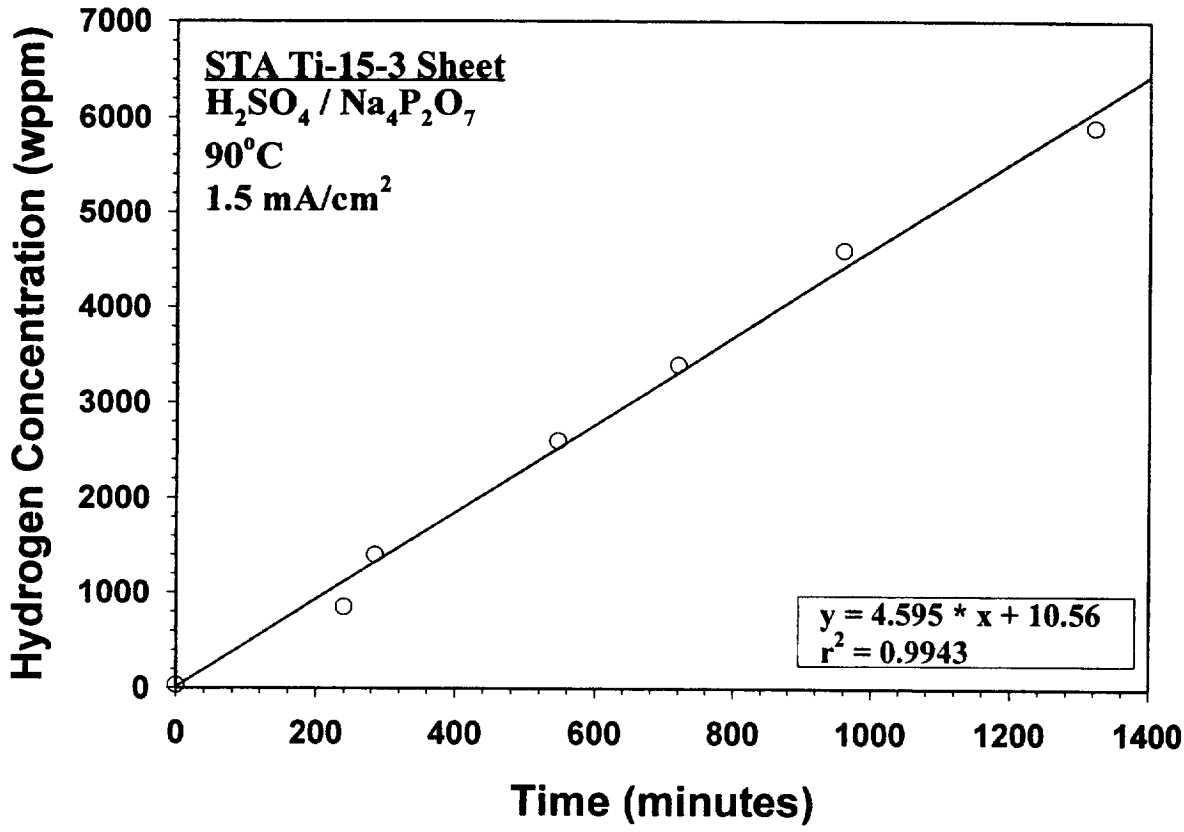

$$\frac{dC_H/dt\ 15\text{-}3}{dC_H/dt\ LCB} = \frac{4.595}{1.668} = 2.755$$

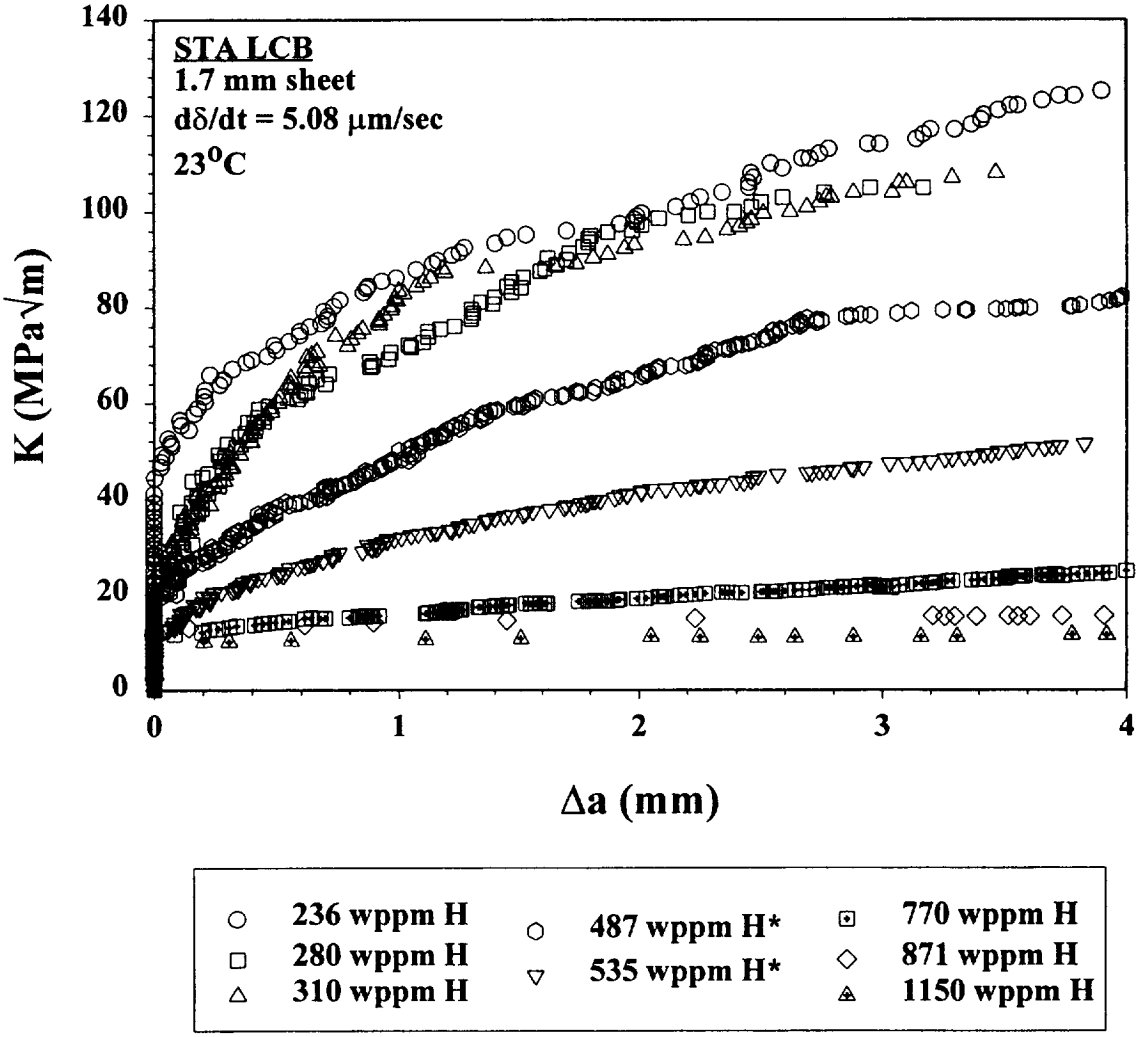
STA LCB
1.7 mm sheet
dδ/dt = 5.08 μm/sec
23°C
K (MPa√m)
Δa (mm)
0
20
40
60
80
100
120
140
0
1
2
3
4
236 wppm H
280 wppm H
310 wppm H
487 wppm H*
535 wppm H*
770 wppm H
871 wppm H
1150 wppm H

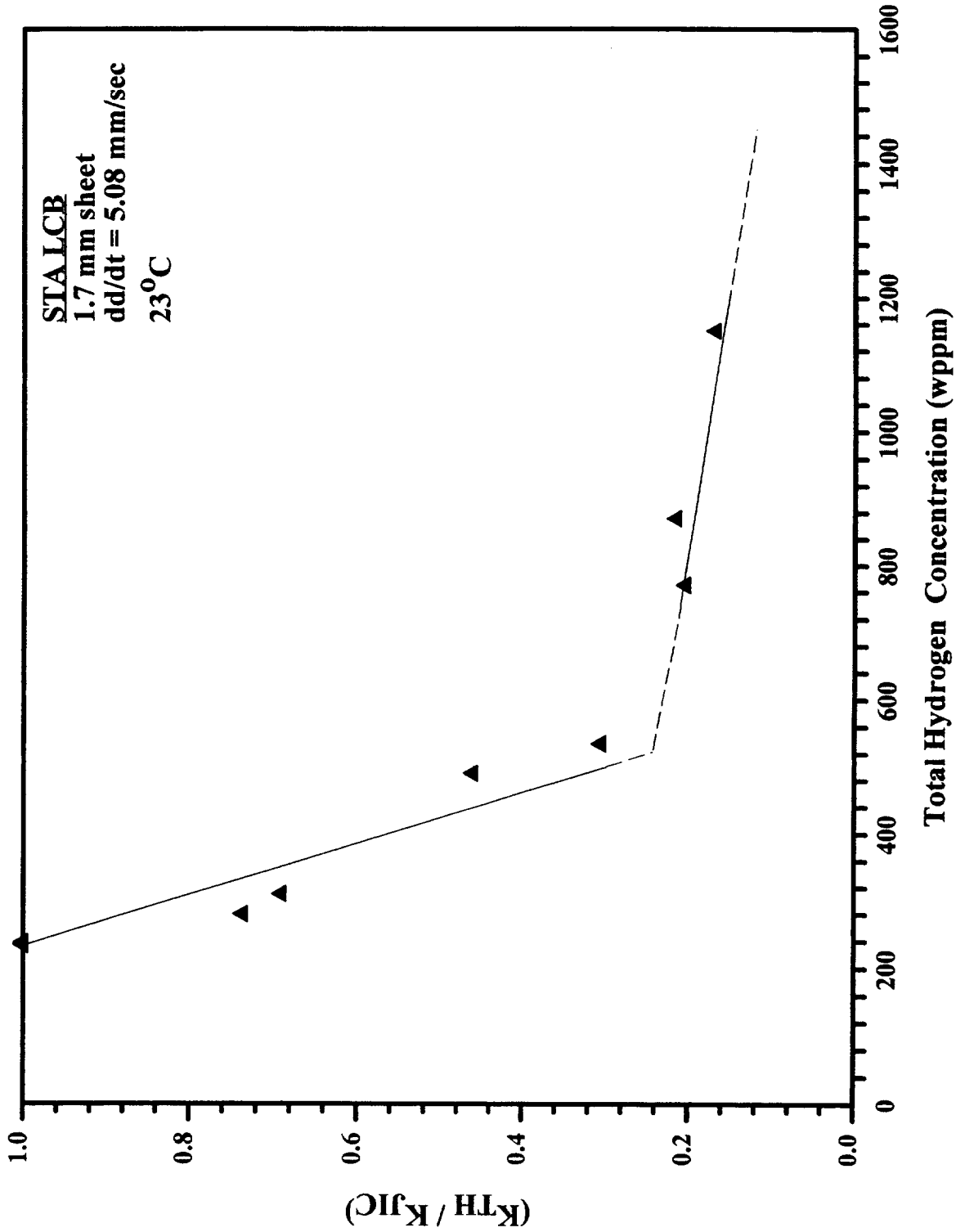
STA LCB
1.7 mm sheet
dd/dt = 5.08 mm/sec
23°C
(KTH / KJIC)
Total Hydrogen Concentration (wppm)
0.0
0.2
0.4
0.6
0.8
1.0
0
200
400
600
800
1000
1200
1400
1600

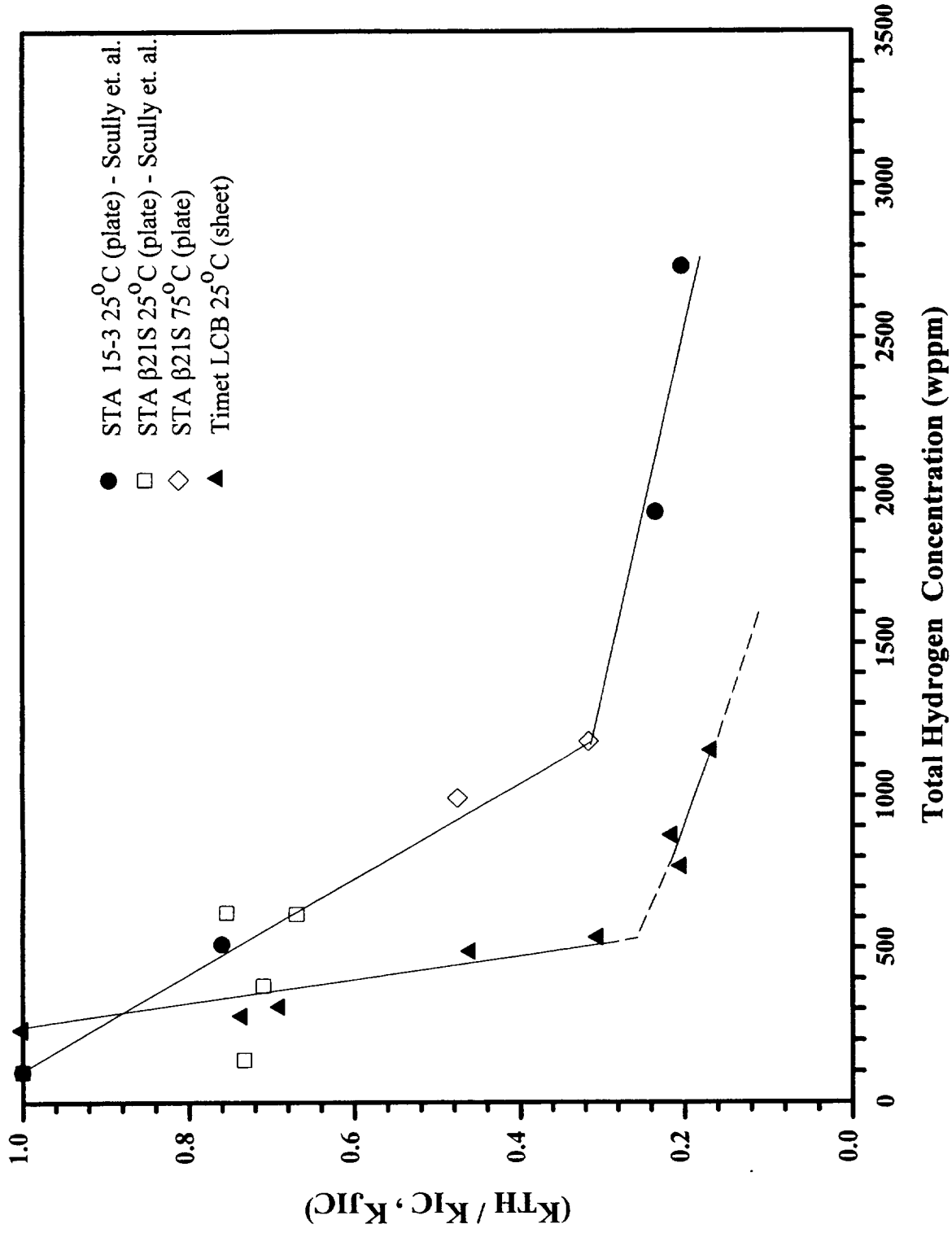
STA 15-3 25°C (plate) - Scully et. al.
STA β21S 25°C (plate) - Scully et. al.
STA β21S 75°C (plate)
Timet LCB 25°C (sheet)
(KTH / KIC , KJIC)
Total Hydrogen Concentration (wppm)
0.0
0.2
0.4
0.6
0.8
1.0
0
500
1000
1500
2000
2500
3000
3500

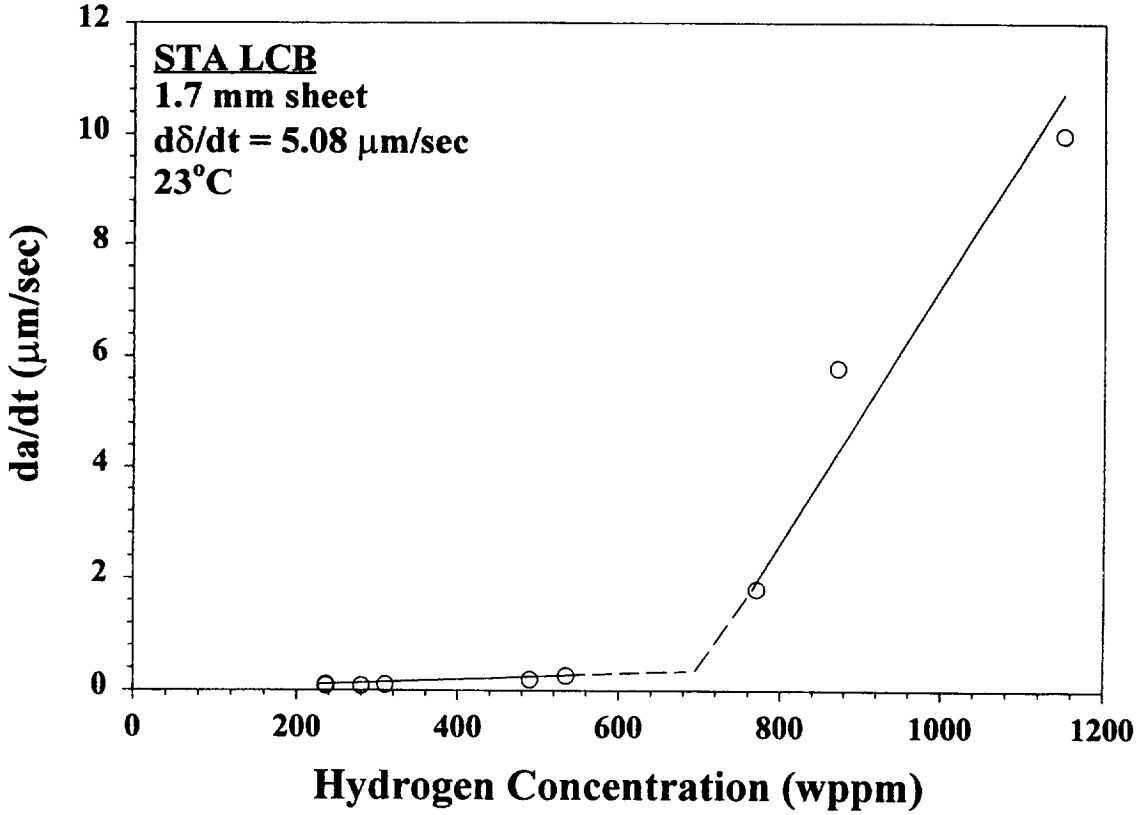
STA LCB
1.7 mm sheet
dδ/dt = 5.08 μm/sec
23°C
da/dt (μm/sec)
Hydrogen Concentration (wppm)
0
2
4
6
8
10
12
0
200
400
600
800
1000
1200

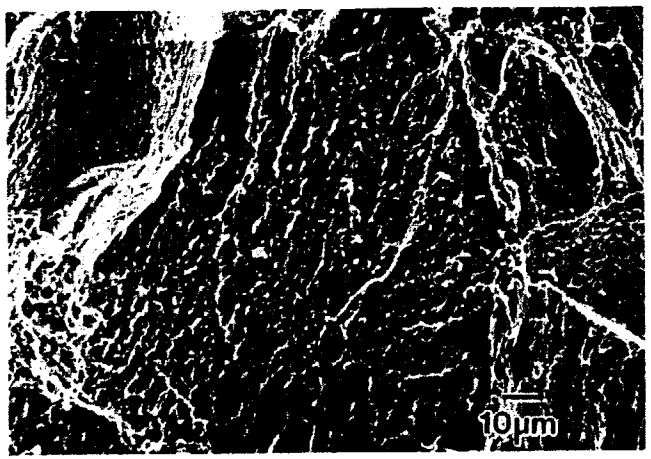

236 wppm
K_{JIC} = 58.2 MPa√m

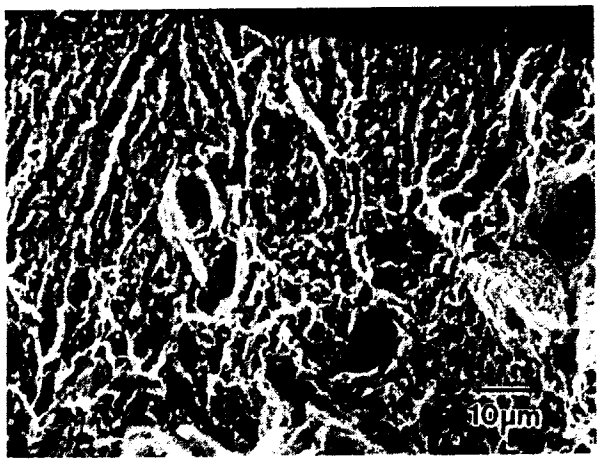

280 wppm
K_{JIC} = 42.9 MPa√m

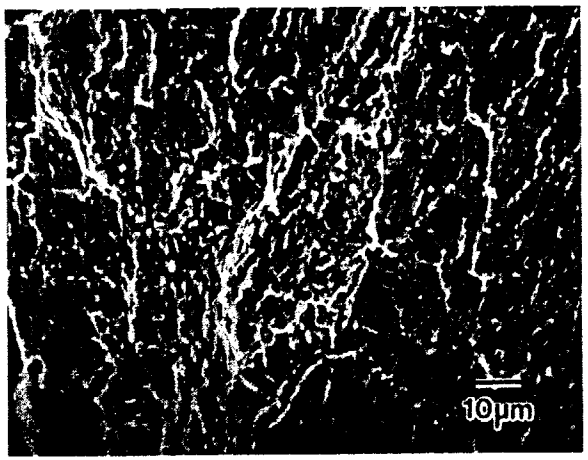

310 wppm
K_{JIC} = 40.2 MPa√m

490* wppm

K_{JIC} = 26.8 MPa√m

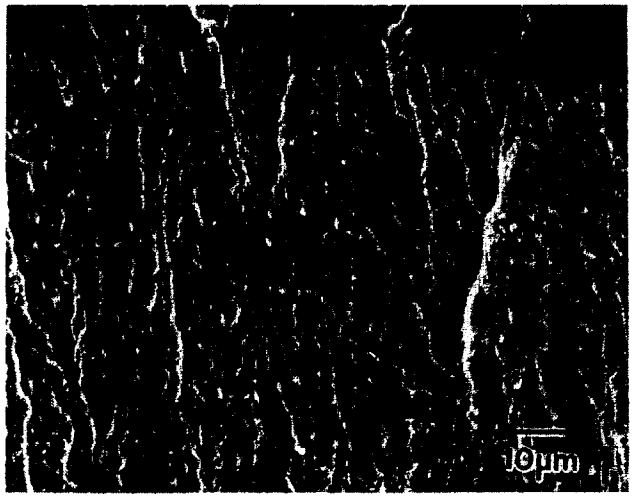

535* wppm

K_{JIC} = 17.8 MPa√m

770 wppm

K_{JIC} = 11.9 MPa√m

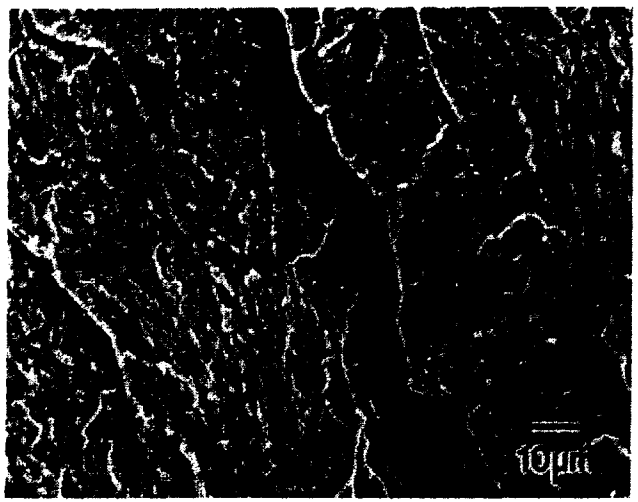

1150 wppm

K_{JIC} = 9.8 MPa√m

Timet LCB sheet Room Temperature Results

Specimen	Hydrogen (wppm)	J_{IC} (kJ/m^2)	K_{JIC} (MPa$\sqrt{m}$)	J_{ICi} (kJ/m^2)	K_{JICi} (MPa$\sqrt{m}$)	K_{ICi} (MPa$\sqrt{m}$)	da/dt (mm/sec)
Sheet 16	A.R.	32.7	64.0	13.1	40.6	40.6	8.1×10^{-5}
Sheet 17	A.R.	23.0	54.0	9.7	34.9	34.9	1.0×10^{-4}
Sheet 18	A.R.	25.5	56.7	12.2	39.1	39.1	1.0×10^{-4}
Sheet 21	280	14.6	42.9	3.3	20.5	20.5	7.8×10^{-5}
Sheet 20	310	12.8	40.2	3.7	21.6	21.6	9.3×10^{-5}
Sheet 22	490*	5.7	26.8	3.0	19.5	19.5	1.9×10^{-4}
Sheet 19	535*	2.5	17.8	1.2	12.0	12.0	2.6×10^{-4}
Sheet 12	770	1.3	11.9	0.9	10.7	10.8	1.8×10^{-3}
Sheet 9	871	1.5	12.5	1.2	11.8	11.8	5.8×10^{-3}
Sheet 10	1150	0.9	9.8	0.8	9.8	9.8	1.0×10^{-2}

Conclusions

- The improved dcPD J-R curve method is effective in detecting crack-growth initiation and monitoring stable crack growth in high strength β-titanium sheet CT specimens.

- dcPD-detected crack-growth initiation corresponds to approximately 100 μm of crack extension in LCB sheet CT specimens. Substantial damage occurs below K_{JIC}.

- The surface oxide on β-titanium alloys hinders hydrogen uptake at low current densities. Short-term high current density charging and air homogenization effectively introduce low levels of hydrogen.

- Predissolved hydrogen reduces the initiation fracture toughness, increases crack growth rate, and alters the fracture modes of high strength β-titanium alloys.

- LCB sheet is susceptible to embrittlement at hydrogen concentrations which are significantly less than other β-titanium alloys.

Future Work

- Decrease the anomalously high hydrogen concentration in as-received STA LCB to a lower value (~50 wppm) and investigate the effect on fracture resistance.

- Characterize the microstructure and ductile fracture resistance of as-received STA Ti-15-3 sheet.

- Investigate the fracture resistance of STA Ti-15-3 sheet as a function of hydrogen concentration.

- Determine the microscopic character of internal hydrogen embrittlement and investigate the causal mechanism.

Project #2: Mechanisms of Deformation and Fracture in High Strength TitaniumAlloys: Effects of Temperature and Microstructure

Susan M. Kazanjian, Hinrich Hargarter, and E.A. Starke, Jr.

Objectives

The aim of this project is to improve fatigue crack initiation and propagation resistance in the β titanium alloy Ti 15-3 by optimizing the microstructure of the material. The effects of altering solution treatment, cold work and aging parameters on grain size, texture, and α precipitate size and distribution in this alloy will be examined. Fatigue testing and characterization of deformation modes within these various microstructures will allow determination of microstructures which optimize fatigue performance.

Current Status

Initial evaluation of the 0.0055" thick Ti 15-3 foil has been completed. Further study of mechanical properties of this foil will be postponed until investigation of thicker material is complete.

Sheet material, nominally 0.090" thick, was received in September 1996. Microstructure, tensile properties, and texture of the as-received sheet have been examined. Standard solution treated and aged (SA) tensile and fatigue initiation specimens were prepared and tested. Variation in fatigue results prompted re-evaluation of the test configuration. Inherent variability in fatigue initiation data obtained with the open-hole M(T) specimen requires statistical analysis of a large quantity of test results. This approach is not practical using available resources. Consequently, attention will be focused on performing fatigue crack growth rate tests on compact tension specimens of standard ASTM geometry, with W chosen to equal that of the extended compact geometry preferred for HSR research . These tests are currently getting started.

Since initial attempts at duplex aging produces specimens of tensile strength much lower than expected, duplex and triplex heat treatments are continuing. Quench rates and aging times will be compared to those used by other researchers to assure that sufficient excess vacancies are present for α precipitation and that over-aging does not occur.

Recent Results

Standard solution treated and aged (SA) tensile and fatigue specimens were prepared by solution treating tantalum-wrapped specimens at 800°C for 1 hour in a flowing argon atmosphere, then quenching in flowing helium (1.0 to 1.5°C/sec). This was followed by aging at 538°C for 8 hours in argon and quenching in helium (0.6 to 1.2°C/sec) to produce acicular α distributed within the beta grains. Tensile yield strength ranged from 140 to 155 ksi between the separate heat treat lots, while elongation varied from 15.1 to 13.8, correspondingly.

Duplex aged (SDA) tensile and fatigue specimens were solution treated at 800°C for 1 hr, quenched, then aged at 600°C for 20 hr, quenched, and aged again at 400°C for 75 hr. This produced a uniform distribution of acicular α phase within the β grains as well as a high volume of continuous α at the grain boundaries. Combined with low tensile results, this unexpected microstructure indicates some deviation in the heat treatment procedure from that reported in the literature. The 20 hour exposure at 600°C appears to be far too long to optimize properties.

Fatigue initiation tests on SA material were conducted at ratios of applied stress to yield stress (YS) of 0.62 to 0.88, R=0.1, 15 Hz. Although specimens tested at 87% and 88% YS showed reasonable agreement (both initiating fracture before 10^5 cycles), specimens tested below 85% YS exhibit widely scattered results. Examination of the fracture surfaces revealed a clear crystallographic dependency of the crack paths, however the cracks were not confined to grain boundaries or immediately adjacent regions.

Future Plans

Heat treatment and thermo-mechanical processing (TMP) of material will continue according to the parameters in the test matrix. Fatigue crack growth rate will be measured for each type of microstructure produced only after consistent tensile properties and microstructures are generated.

Electron microscopy will be used to further investigate the crystallographic dependence of crack propagation recognized in the initiation specimens. It will be

interesting to determine the influence of the rolling TMP's on texture and, subsequently, on fatigue crack propagation.

In addition, the fractured tensile and FCGR specimens will be examined under electron microscopy in an effort to characterize the deformation taking place during testing.

Presentation Captions

1. Title
2. β-Ti research goals include determination of the effect of microstructure and crystallographic texture on deformation and fatigue behavior.
3. This fatigue investigation will identify factors which optimize fatigue resistance in Ti 15-3.
4. The test matrix of thermo-mechanical heat treatment was developed to reproduce conditions which other researchers have identified as offering good combinations of tensile and fracture toughness properties.
5. Experimental plan.
6. Characterization of as-received Ti 15-3 0.092" (nom.) sheet: optical microscopy and x-ray diffraction.
7. The texture of the as-received material is relatively low as shown by pole figures of {100}, {200}, and {211} poles.
8. Texture of as-received sheet, orientation distribution function.
9. Tensile properties. Results for as-received sheet indicate some anisotropy.
10. Characterization of solution treated and standard aged (SA) material. Fine acicular α is evident within the β grains.
11. Tensile tests on SA sheet reveal a small amount of variation, due possibly to slight deviation in heat treatment temperatures between lots.
12. Fatigue initiation data. Data measured on SA sheet proved too widely scattered to draw any significant conclusions.
13. Fatigue initiation graph: cycles to initiation v. applied stress as a fraction of yield stress.

14. Fatigue crack surface topography.
15. Fatigue crack path, cross-section showing crystallographic dependence of crack propagation.
16. Duplex aged microstructure.
17. Effect of cold work on α morphology. Cold work prior to aging distributes dislocations throughout the β grains to provide a homogeneous distribution of nucleation sites for α precipitation.
18. Effect of cold work (continued). Structures reported by other researcher.
19. Effect of crystallographic orientation. Crystallographic texture within the β matrix due to cold work may affect the fatigue properties. Orientation of the precipitated phase to the matrix may also control slip length which can influence fatigue resistance.
20. Effects of grain size and vacancy concentration will be removed from this part of the study by maintaining constant solution treatment temperature, time and quench rate.
21. Summary.
22. References.

Deformation, Fracture and Fatigue of High Strength Beta-Titanium Alloys

University of Virginia
Materials Science and Engineering
Light Alloys Group

S. Kazanjian, H. Hargarter and E. A. Starke

UVA β-Ti Research Goals

- **Microstructural Development**
  - Identify the effects of altering solution treatment, rolling and aging conditions on grain size, texture and alpha precipitate size and distribution.
- **Deformation Characterization**
  - Examine the interactions of dislocations with microstructural features.
- **Fatigue Investigation**
  - Determine the influence of grain size, texture and alpha precipitate morphology on fatigue crack initiation and propagation.

Fatigue Investigation

- From work performed by others, we know that α size, shape, and distribution and β grain size can affect:
  - Slip length
  - Slip character (wavy or planar)/
  - Strain localization
  - Dislocation pile-up strength

  All of which influence fatigue performance.
- α Morphology in Ti 15-3 depends on:
  - Cold Work Prior to Aging
  - Aging Procedures and Temperatures (TMP)
  - Prior β Grain size
  - Solution Treatment Temperatures

TMP Conditions

Condition	Temp/Time	Resulting Microstructure	Tensile		Benefits
	T1/t1 (°C) / (hr)		UTS (MPa)	% Elong	
Solution Treated (S)	800/1	Entirely beta	780	23	
Standard Age (A)	540 / 8	Lathe alpha ppt on g.b.'s and within β grains. PFZ's along g.b.'s	1000	14	
Duplex Age (DA)	600 / 14 to 28 400 / 50 to 100	Bimodal distribution of coarse and fine α ppt within β grains			Enhances fracture toughness by creating tortuous crack path.
Triplex Age (TA)	300 / 10 600 / 3 to 6 450 / 100	Homogeneously distributed coarse α ppt prior to high-low aging			Reduces benefit of duplex age on fract. toughness, presumably due to increased homogeneity of microstructure.
60%CR + Age (CRA)	540 / 8	Lathe shaped α within β grains. Reduces g.b. ppt of α by providing dislocations as homogeneously distributed nucleation sites.	1200	10	Increases strength without loss of ductility. Increases rate of strengthening, reducing required aging times.
60% WR, 600°C+ Age (WRA)	540 / 8				

Experimental Plan

- Characterize as-received material - Completed
  - Texture
  - Microstructure
  - Tensile properties
- Characterize heat treated material
  - Tensile deformation modes, TEM/SEM-12/96-1/97
  - Fatigue initiation, center hole specimen - 12/96
  - Fatigue propagation, extended compact specimen, DCPD - 7/97-12/97
  - TEM on fatigued specimens - 7/97-12/97
- Characterize TMP'd material
  - tensile properties - 8/97-12/97
  - fatigue propagation and TEM- 9/97 - 12/97

Characterization of As-Received Ti 15-3

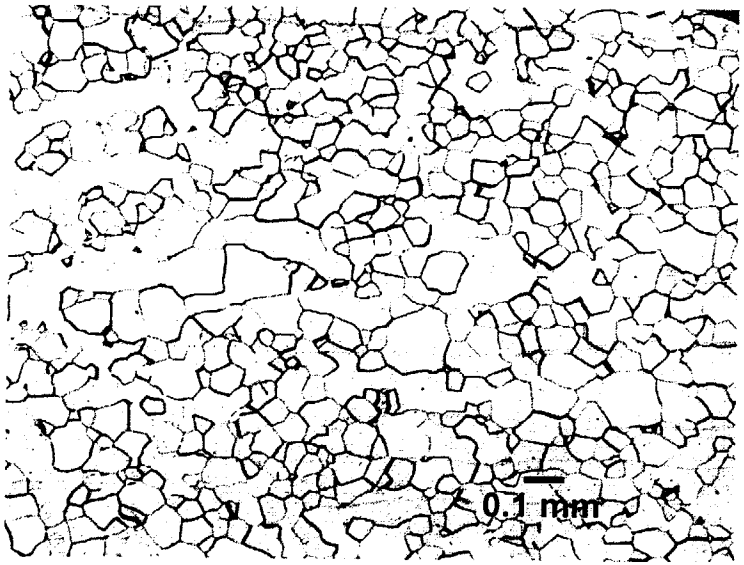

Optical microscopy reveals grain size on the scale of 100 microns.

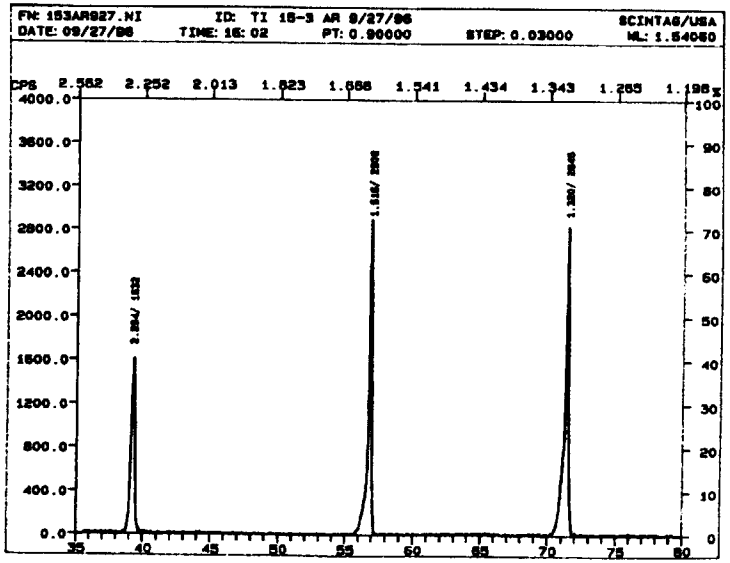

X-ray diffraction of the sheet exposed only those peaks characteristic of the beta phase.

Texture of As-Received Ti 15-3

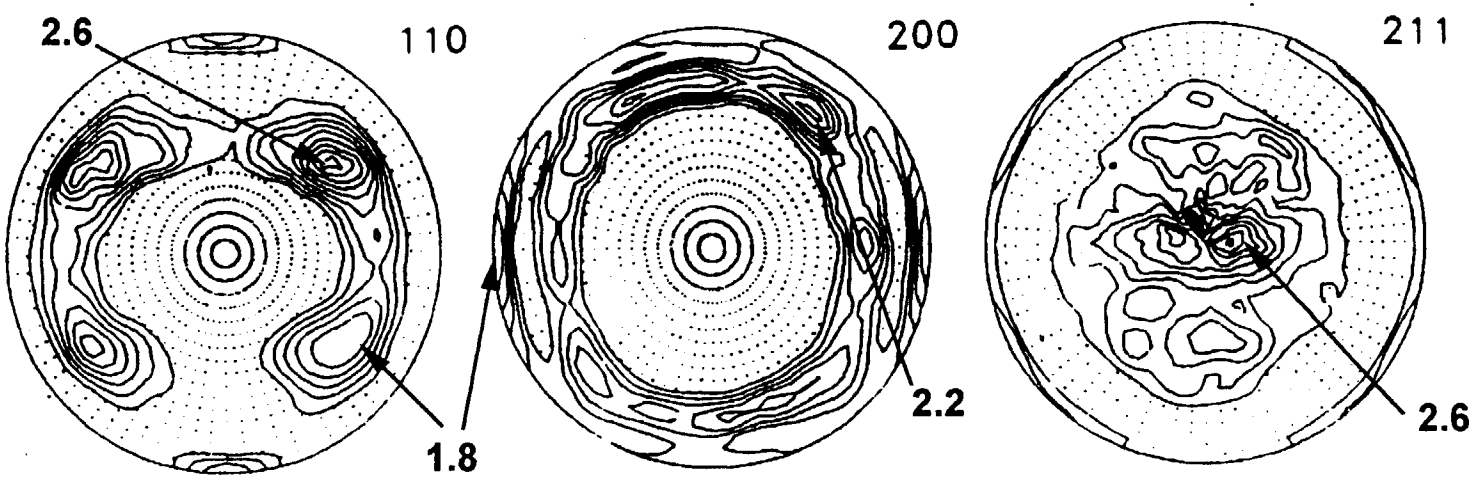

Individual $\{110\}_{beta}$, $\{200\}_{beta}$ and $\{211\}_{beta}$ pole figures measured on the 0.090 inch sheet in the as-received condition.

Texture of As-Received Ti 15-3

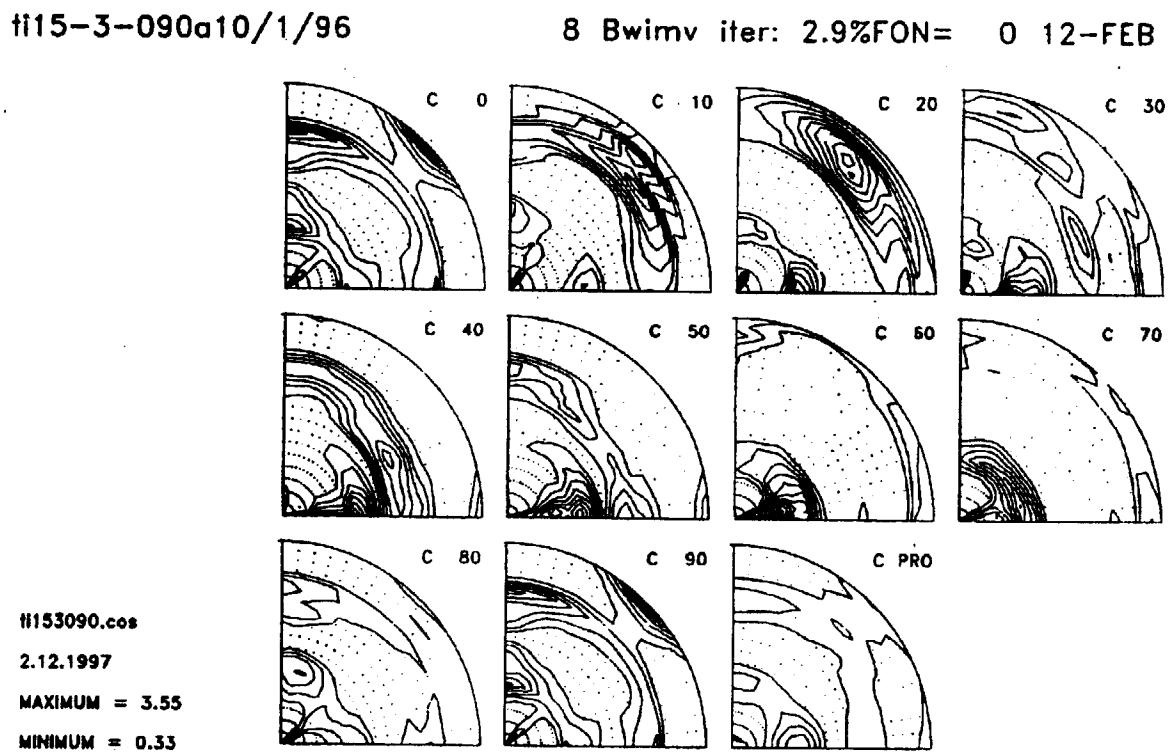

Orientation Distribution Function

Tensile Properties of Ti 15-3 Material

Condition	Designation		YS ksi/ MPa	UTS ksi/ MPa	% Elong
	HT	Lot-Orient.			
As-received	R	L	107/739	107/739	22.2
		T	111/766	111/766	22.3
Sol'n Treated 800°C, 1hr	S	D-L	110/758	112/768	22.5
S+Age	SA	E-L	140/965	152/1052	15.1
800°C, 1hr	SA	F-L	146/1010	159/1096	13.2
538°C, 8hr	SA	G-L	152/1048	162/1117	14.1
	SA	H-L	144/988	156/1077	13.6
800°C, 1 hr 600°C, 20 hr 400°C, 75 hr	SDA	I-L	131/906	146/1006	17.2

Standard Aging

Aging for 8 hours at 538 °C is expected to produce a uniform distribution of alpha phase within the beta matrix.

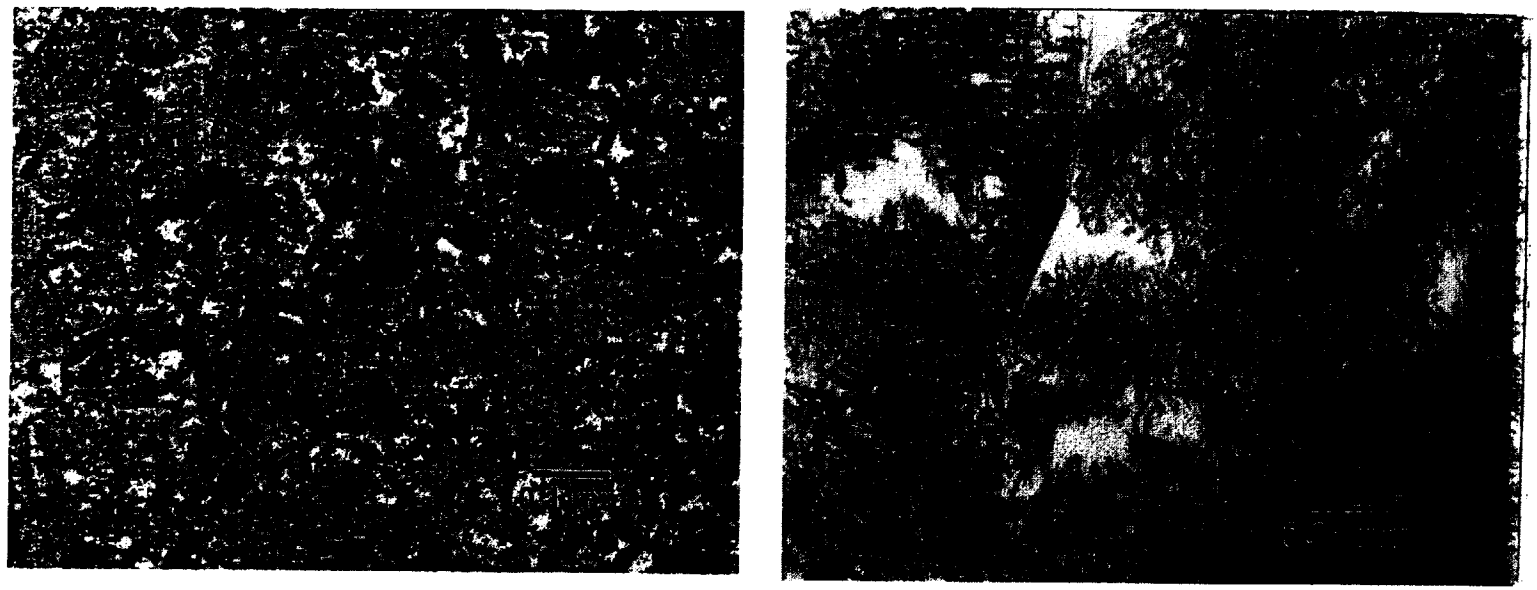

(a) **(b)**

SA microstructures, solution treated, 800°C, 1 hr then standard aged, 538°C , 8 hrs, s-t orientation, (a) low magnification, (b) high magnification.

Tensile Properties of Ti 15-3 Material

Condition	Designation		YS ksi/ MPa	UTS ksi/ MPa	% Elong
	HT	Lot-Orient.			
As-received	R	L	107/739	107/739	22.2
		T	111/766	111/766	22.3
Sol'n Treated 800°C, 1hr	S	D-L	110/758	112/768	22.5
S+Age	SA	E-L	140/965	152/1052	15.1
800°C, 1hr	SA	F-L	146/1010	159/1096	13.2
538°C, 8hr	SA	G-L	152/1048	162/1117	14.1
	SA	H-L	144/988	156/1077	13.6
800°C, 1 hr 600°C, 20 hr 400°C, 75 hr	SDA	I-L	131/906	146/1006	17.2

Cycles to Initiation, SA Ti 15-3

R = 0.1, frequency = 15 Hz

Specimen	YS (MPa)		YS (ksi)	Elong. %	Conc. Factor	Max Applied Load (lbs)	Applied Stress /YS	Cycles to Initiation	
IB1	1000	(nom)	145		3.15	3600	0.84	> 6.60E+06	
IB2	1000	(nom)	145		3.15	3400	0.80	> 5.23E+06	
IC1	1000	(nom)	145		3.15	3730	0.87	5.60E+04	
IC2	1000	(nom)	145		3.15	3730	0.88	3.18E+04	
IC3	1000	(nom)	145		3.15	3000	0.70	> 2.70E+05	
IF2	1096		159	13.3	3.15	3683	0.79	3.97E+04	
IF3	1096		159	13.3	3.15	2880	0.62	> 1.00E+07	
IF4	1096		159	13.3	3.15	3260	0.70	4.36E+04	
IG1	1116		162	14.0	3.15	3580	0.75	> 3.72E+06	
IG2	1116		162	14.0	3.15	3580	0.75	> 1.23E+07	
IG3	1116		162	14.0	3.15	3827	0.80	> 3.55E+06	*
IG4	1116		162	14.0	3.15	3832	0.80	> 1.00E+07	
IG5	1116		162	14.0	3.15	specimen flawed- not tested			

* Overloaded to .86 YS (in fatigue) during set-up.

Cycles to Initiation, SA Ti 15-3

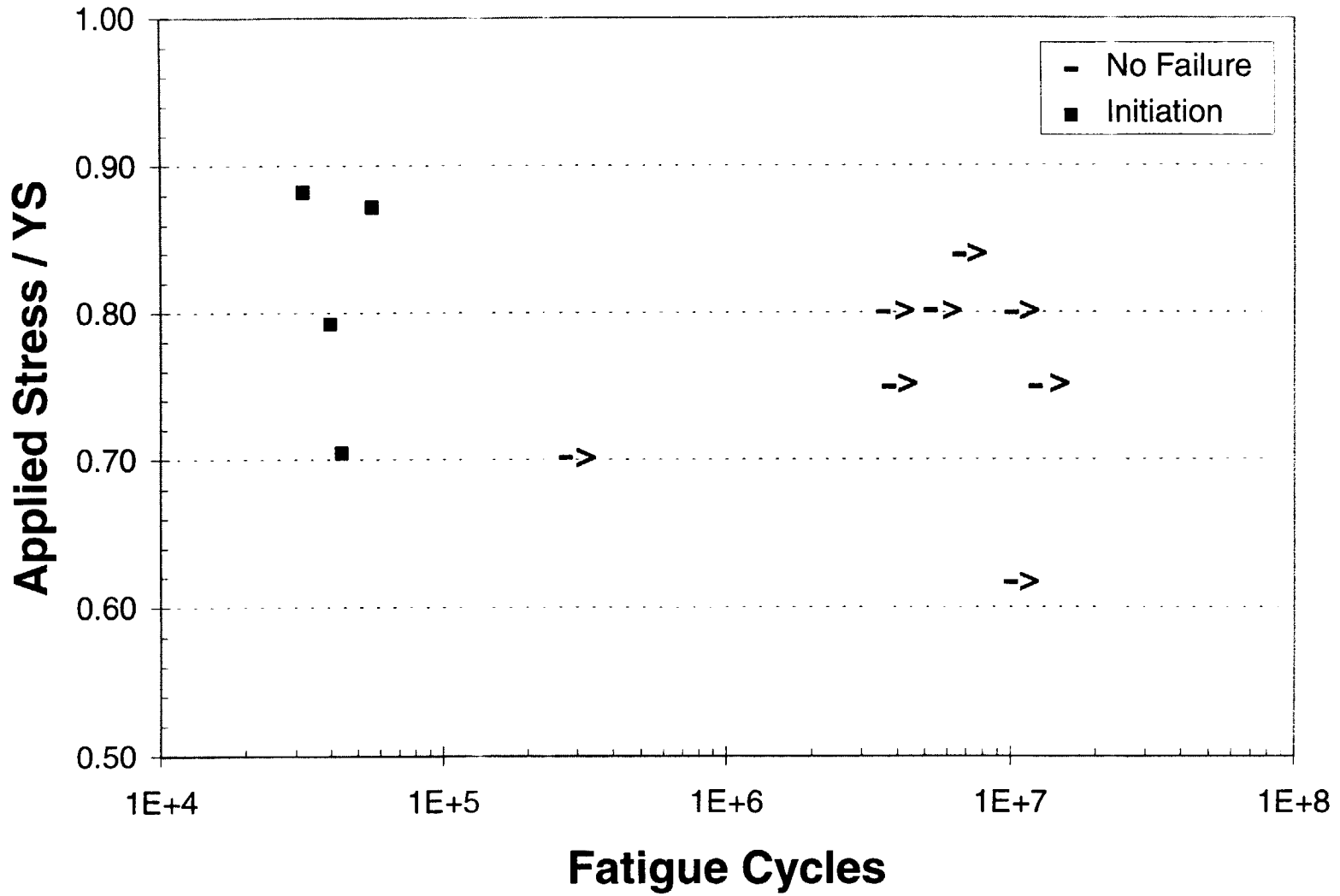

Fatigue Initiation Site, SA Ti 15-3

R = 0.1, frequency = 15 Hz, Specimen IF2

(a)

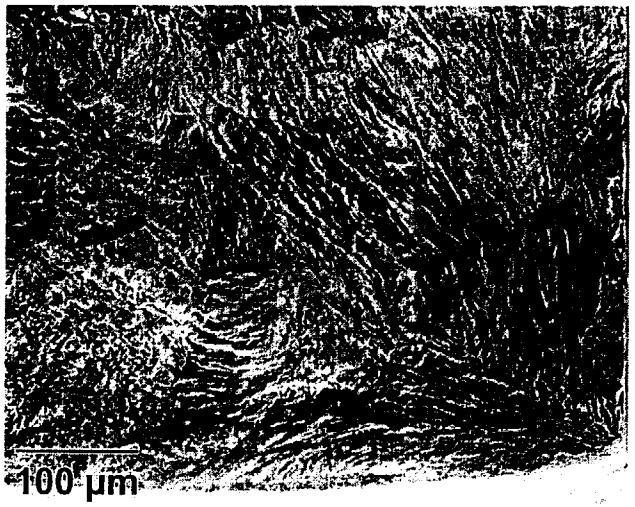

(b)

SEM view of fracture surface, specimen IF2. Initiation occurred in lower right corner. (a) low magnification, (b) high magnification. Both views show that fatigue crack propagation is transgranular with a crystallographic dependence. The crack changes plane between grains, but is not confined to grain boundaries.

Fatigue Crack Path, Cross-Section

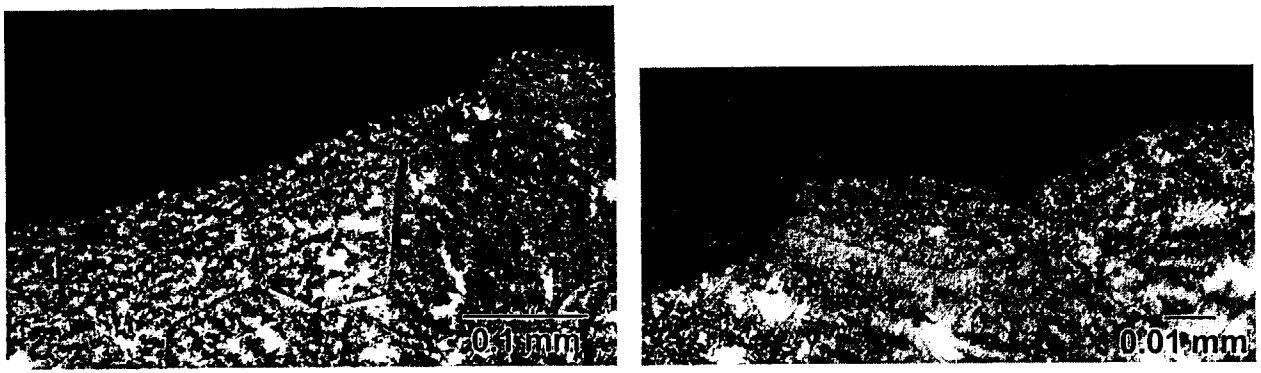

(a) (b)

Cross section of fracture surface near (not at) initiation site, specimen IF2, (a) low magnification, (b) high magnification.

Duplex Aging

High T/ Low T aging is expected to produce a bimodal structure of coarse and fine alpha in the beta matrix.

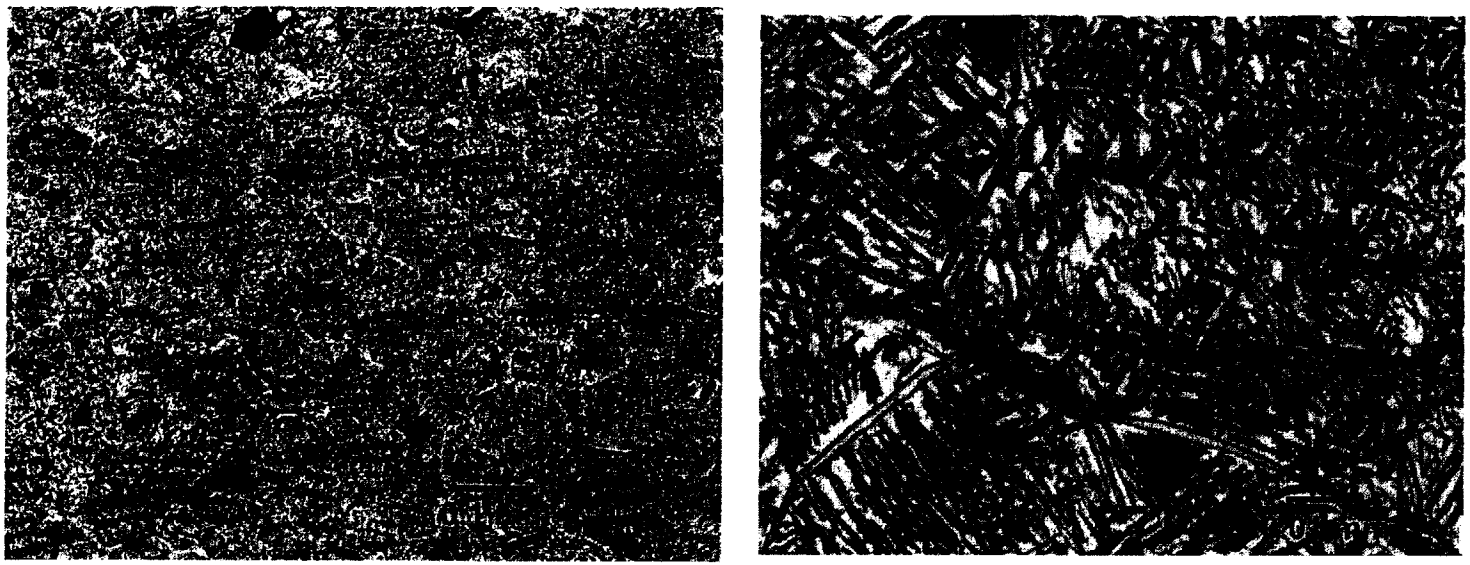

(a) (b)

SDA microstructures, solution treated, 800°C, 1 hr then duplex aged, 600°C , 20 hrs followed by 400°C, 75 hrs, l-t orientation, (a) low magnification, (b) high magnification.

Effect of Cold Work on α Morphology

- Cold work prior to aging distributes dislocations throughout the β grains to provide a homogeneous distribution of nucleation sites for α precipitation.
  - 0% => preferential α precipitation on grain boundaries with α lathes within b grains
  - <50% => preferential α precipitation at dislocations as well as grain boundaries.
  - >50% => α precipitation predominantly at β subgrain boundary nodes
  - 80% => α + β microduplex structure with very fine β subgrains and α particles.

Effect of Cold Work

- **Light to medium deformation. Imam, Poulose and Rath, NRL 1993**

showing alpha precipitates and deformation band.

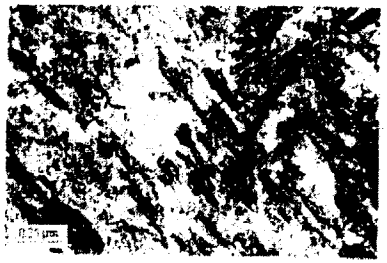

- **Heavy deformation. Inaba, Ameyama and Tokizane,1991**

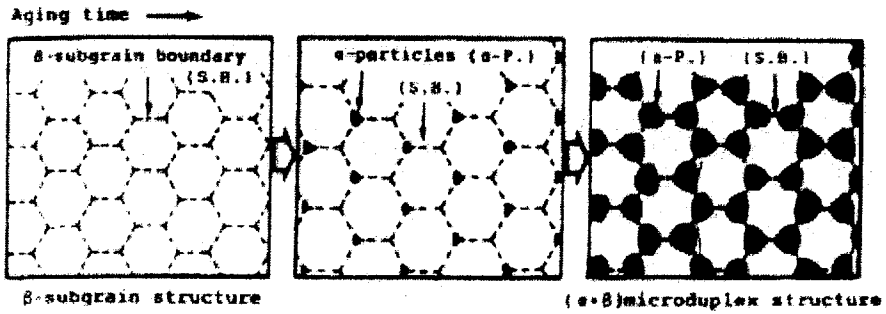

Fig. 10. Schematic drawing of the formation process of $(\alpha - \beta)$ microduplex structure.

Crystallographic Orientation

- Cold rolling produces strong textures with respect to the rolling direction
- Orientation of α to β matrix can affect slip length.

Solution Treatment Temperature

- **Excess Vacancy Concentration**
  - **Higher with**
    - » **Higher Temperature prior to Quench**
    - » **Larger Grain Size**
  - **High Concentration=>Homogeneous**
  - **Low Concentration=>Inhomogeneous**
- **Grain Size**

Summary

- Widely scattered fatigue initiation results prompted the suspension of fatigue testing on the Ti 15-3 open-hole M(T) specimen.
- FCGR measurement of Ti 15-3 specimens of C(T) geometry with W = 1.2, B = 0.035 is beginning.
- Fractured tensile and FCGR specimens will be examined by SEM and TEM to determine the nature of deformation taking place.
- The crystallographic dependency of fatigue crack propagation will also be investigated.

References

① M. A. Imam, P. K. Poulose and B. B. Rath, "Modification of Alpha Phase Precipitation by Cold Work of the Ti-15-3 Alloy", *Beta Titanium Alloys in the 1990's,* ed. D. Eylon, R. Boyer and D. Koss, TMS, 1993.

② T. Inaba, K. Ameyama and M. Tokizane, "Formation of (a + b) Microduplex Structure in a Ti-15V-3Cr-3Sn-3Al Alloy", *ISIJ International,* v. 31 (1991), no. 8, pp 792-798.

③ M. Okada, "Strengthening of Ti-15V-3Cr-3Sn-3Al by Thermo-mechanical Treatments", *ISIJ International,* v. 31 (1991), no. 8, pp 834-839.

④ H. Fujii and H. G. Suzuki, "Effect of Quenched-In Vacancies on Aged Microstructures in Ti-15V-3Cr-3Sn-3Al", *Materials Transactions, JIM,* v. 34, no. 4 (1993), pp. 382-388. (Originally pub. in Japanese in 1991)

⑤ Niwa and Takatori, "Effect of Step-Aging on the Fracture Toughness of Ti-15v-3Cr-3Sn-3Al Alloy", *Beta Titanium Alloys in the 1990's,* ed. D. Eylon, R. Boyer and D. Koss, TMS, 1993, p 237-247.

Project 3: Creep Behavior and Microstructural Stability of Al-Cu-Mg-Ag and Al-Li-Mg-Ag Alloys.

Susan M. Kazanjian, Ning Wang and E.A. Starke

Objective and Experimental Approach

This project focuses on understanding the creep behavior of the aluminum alloys C415 and C416, both of composition Al-Cu-Mg-Ag, and ML377, an Al-Cu-Li-Mg-Ag alloy. The creep response of these alloys are being compared to that of CM.001 (2618) which is currently in use on the supersonic Concorde. Creep strains are being measured under conditions originally predicted to be imposed by Mach 2.0-2.2 service, but now considered by NASA to be of general interest to many flight applications. Microstructural evolution in the vicinity of the grain boundaries of these alloys is being examined directly in the transmission electron microscope (TEM) and by fracturing crept specimens at cryogenic temperatures to expose grain facets. Variation in number density and size of grain boundary precipitates as the severity of creep conditions increases are being related to creep behavior. The significance of the various different phases precipitated by the alloys of different compositions is also being investigated.

Current Status

Creep curves under the various conditions tested provide data for direct assessment of the creep resistance of candidate alloys. Tests are continuing on CM.001 (2618) and C415 to provide long term data under the conditions identified by NASA to be of prime interest, 225°C and 30 ksi. Several more tests are also continuing in order to furnish additional insight into the creep processes.

Cryogenic fracture of all of the specimens removed from creep exposure have been completed. Fracture surfaces have been examined under scanning electron microscopy (SEM) and compared to those of cryogenically fractured alloys which underwent equivalent temperature exposures without stress application. (These thermally exposed materials were provided by NASA.) Optical microscopy has been used to compare grain sizes of all of these materials.

Selected area diffraction pattern (SADP) and TEM examination of specimens before and after creep are currently underway to determine the detailed microstructural changes occurring during creep. This will provide fundamental evidence to characterize creep behavior and degradation mechanisms.

Microhardness measurements at temperatures of interest are also underway to provide supplementary data to correlate microstructural changes with softening or hardening effects.

Recent Results

Strain data measured under the following conditions is currently available:

Alloy	Specimen No.	Temp. (°F)	Stress (ksi)	YSnom (ksi)	Stress/YS
C415	5L-35	275	20	75	0.267
	5L-27	275	25	75	0.333
	5L-28	225	30	75	0.400
C416	6L-33	275	40	72	0.556
	6L-35	225	20	72	0.278
	6L-32	225	30	72	0.417
ML-377	MLL-34	275	25	75	0.333
	MLL-35	275	40	75	0.533
	MLL-32	225	30	75	0.400
CM.001	CM-2	275	30	56	0.536
	CM-1	225	30	56	0.536
	CM-3	225	20	56	0.357

In the T8 temper condition with 2% stretch prior to aging, alloy CM.001 precipitates θ' and S'(on dislocations), C415 precipitates Ω and S'(fine & few), while C416 precipitates Ω and θ'. When present, θ' precipitates on {100} habit planes, while Ω precipitates on {111} planes. It is evident that the creep resistance is greatly enhanced by the presence of the Ω phase in C415 and C416.

C415 is less thermally stable and creep resistant than C416, although C415 possesses higher ambient and elevated temperature strength. The lower thermal stability and creep properties of C415 mainly result from the nucleation and growth of S' on

dislocations. The annihilation of dislocations by S' precipitates reduces the dislocation-induced hardening effect and causes softening of this alloy. This effect is substantiated by the observation that the hardness of alloy decreased and the primary creep rate increased when S' precipitated on dislocations. Creep-induced S' precipitation at grain boundaries had an additional deleterious effect on primary creep of C415.

As S' is the least effective precipitate for strengthening among Ω, θ' and S', increasing the precipitation of S' at the expense of the other two strengthening phases may also contribute to reduced creep resistance. This is currently under investigation.

Future Work

TEM and SADP techniques will be used to study the microstructural development under creep conditions of CM.001 and ML377 alloys, similar to the work done on C415 and C416 described above.

Measurement of microhardness variation with thermal exposure will also continue on all alloys. This will provide time-temperature-transformation (TTT) data valuable for the comparison to crept material.

Additional creep tests are underway at temperatures above those in the previous test matrix in order to determine whether accelerated creep testing is possible for these alloys. The identity and ratios of precipitates which form will be quantified.

Presentation Captions

1. Creep curves of alloy C415, C416, CM.001 and ML-377 (creep tests at 225°F).
2. Creep curves of alloy C415, C416, CM.001 and ML-377 (creep tests at 275°F).
3. The variation of hardness for samples subjected to creep.
4. The variation of hardness for alloy C415 & C416 subjected to thermal exposure or creep.
5. The comparison of creep curves of CM.001, C415 and C416 tested at 275°F.
6. SAED patterns showing the <001>α zone axis from samples of (a) CM.001 in the T8 condition; (b) CM.001 in the crept condition of 275°F-30ksi-3647hr; (c) C415 in the

T8 condition; (d) C415 in the crept condition of 275°F-30ksi-1681hr; (e) C416 in the T8 condition; (f) C416 in the crept condition of 275°F-30ksi-1681hr.

7. Bright-field electron micrographs of alloy C415 and C416 in the T8 condition. (a), (b) the electron beam is approximately parallel to the <011>α direction; (c), (d) the electron beam is approximately parallel to the <001>α direction.
8. Bright-field electron micrographs of alloy C415 and C416 in the crept condition of 275°F-30ksi-1681hr. The electron beam is approximately parallel to the <001>α zone axis.
9. Transmission electron micrographs from alloy C415 crept 1681hr at 275°F, 30ksi, showing: (a) and (b) S or S' precipitates on dislocations and (c) energy dispersive X-ray spectrum recorded from the precipitates.
10. Transmission electron micrographs from alloy C416 crept 1681hr at 275°F, 30ksi, showing: (a) and (b) θ' precipitates on dislocations and (c) energy dispersive X-ray spectrum recorded from the precipitates.
11. Bright-field electron micrographs from alloy C415 in the crept condition of (a), (b) 275°F, 20ksi, 1341hr and (c) 275°F, 30ksi, 1681hr. The operating reflection is {200}α in (a), and the electron beam is approximately parallel to <001>α direction.
12. Bright-field electron micrographs from alloy C415 thermal exposed 3000 hr at 275°F.
13. Transmission electron micrographs of alloy C415, showing precipitates within the grain boundary region, (a) prior to creep, (b) thermal exposed 3000hr at 275°F, (c) crept 1341hr at 275°F, 20ksi and (d) crept 1681hr at 275°F, 30ksi.
14. Bright-field electron micrographs from alloy CM.001 prior to creep. The electron beam is approximately parallel to <001>α zone axis.
15. Bright-field electron micrographs from CM.001 crept 3647 hr at 275°F, 30ksi . The electron beam is approximately parallel to <011>a zone axis.
16. Transmission electron micrographs of alloy CM.001, showing precipitates within the grain boundary region (a) prior to creep; (b) crept 3647hr at 275°F, 30ksi.
17. Summary

Creep Behavior and Microstructural Stability of Al-Cu-Mg-Ag and Al-Li-Mg-Ag Alloys

Susan M. Kazanjian, Ning Wang and E.A. Starke
Light Metals Center
School of Engineering & Applied Science
University of Virginia
Charlottesville, VA 22903

The objective of the project

- Develop an understanding of the relationship between microstructural features and mechanical properties with the creep behavior of the aluminum alloys C415, C416 and ML377.
- Compare the creep response of these alloys with CM.001(2618) which is currently in use on the supersonic Concorde.

Modified 2519 (C415 & C416)

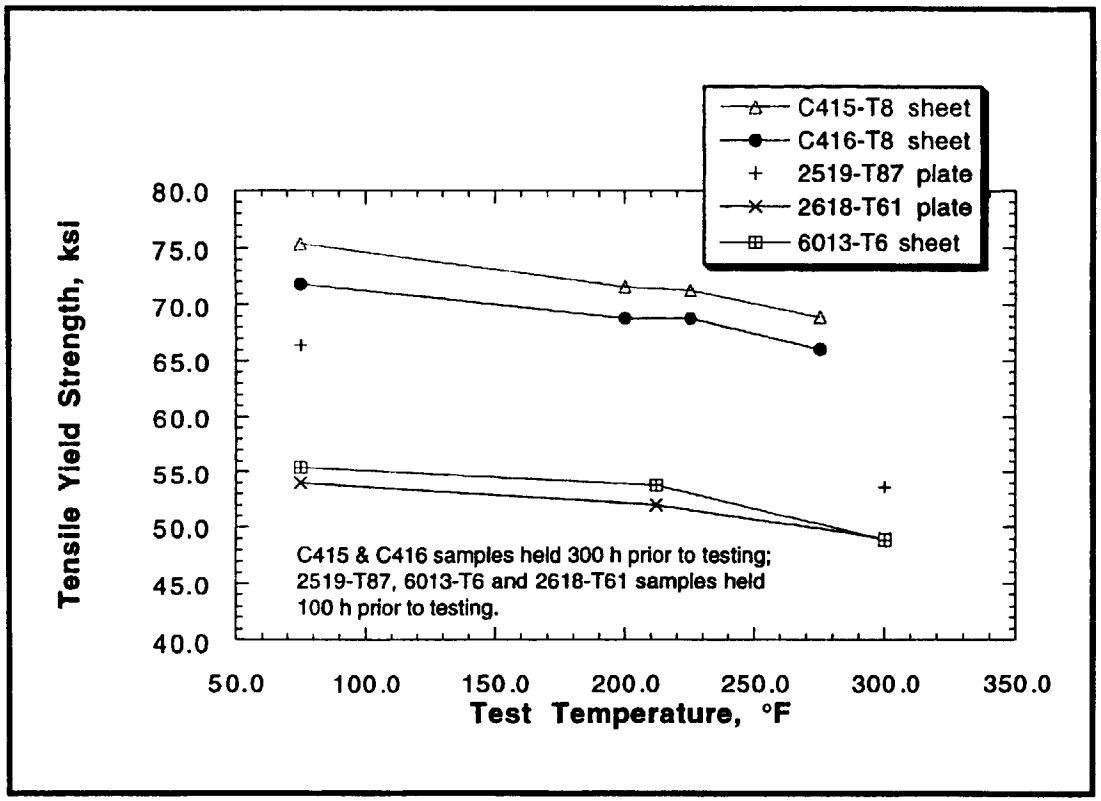

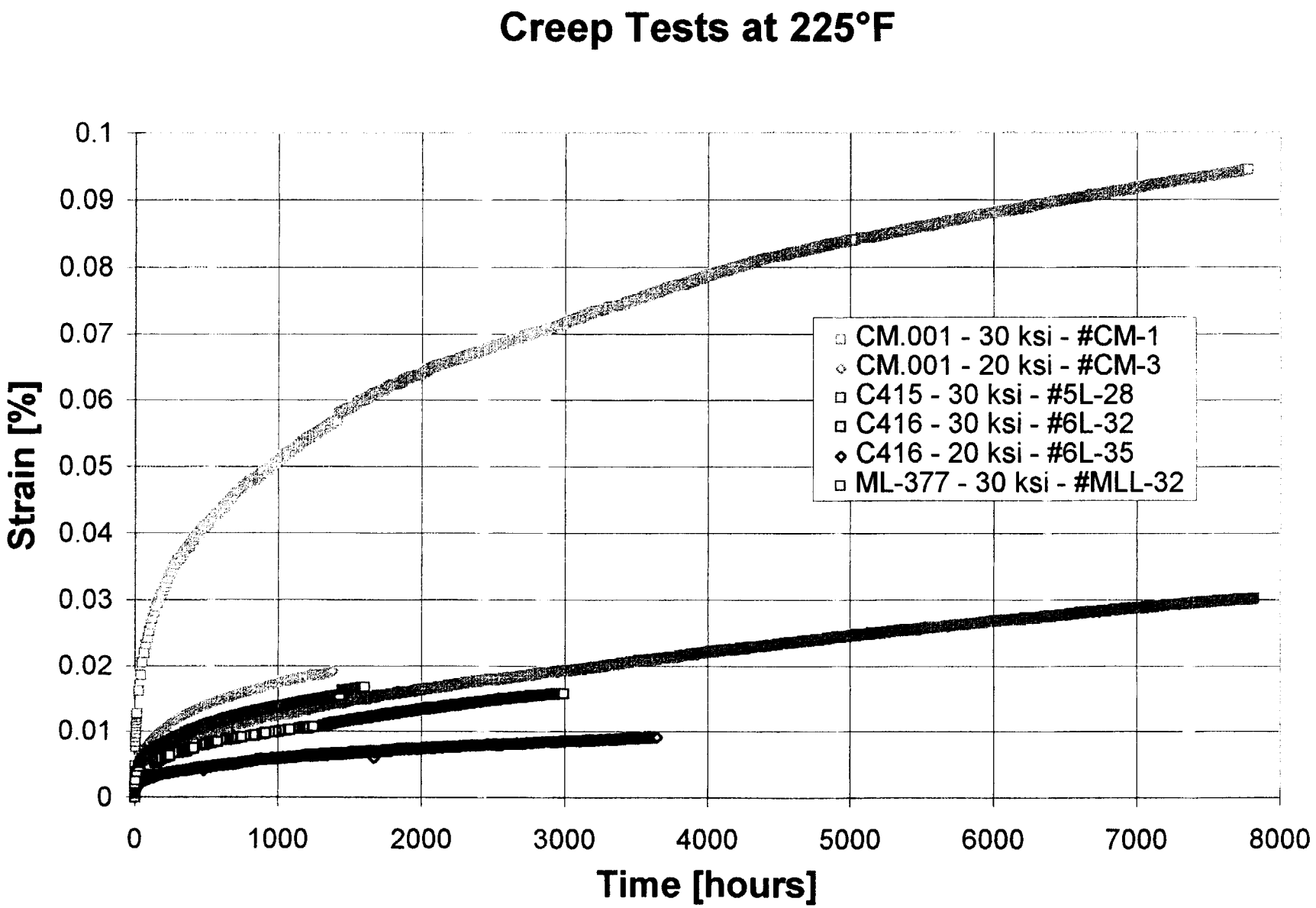
Creep Tests at 225°F
Strain [%]
0.1
0.09
0.08
0.07
0.06
0.05
0.04
0.03
0.02
0.01
0
0
1000
2000
3000
4000
5000
6000
7000
8000
Time [hours]
CM.001 - 30 ksi - #CM-1
CM.001 - 20 ksi - #CM-3
C415 - 30 ksi - #5L-28
C416 - 30 ksi - #6L-32
C416 - 20 ksi - #6L-35
ML-377 - 30 ksi - #MLL-32

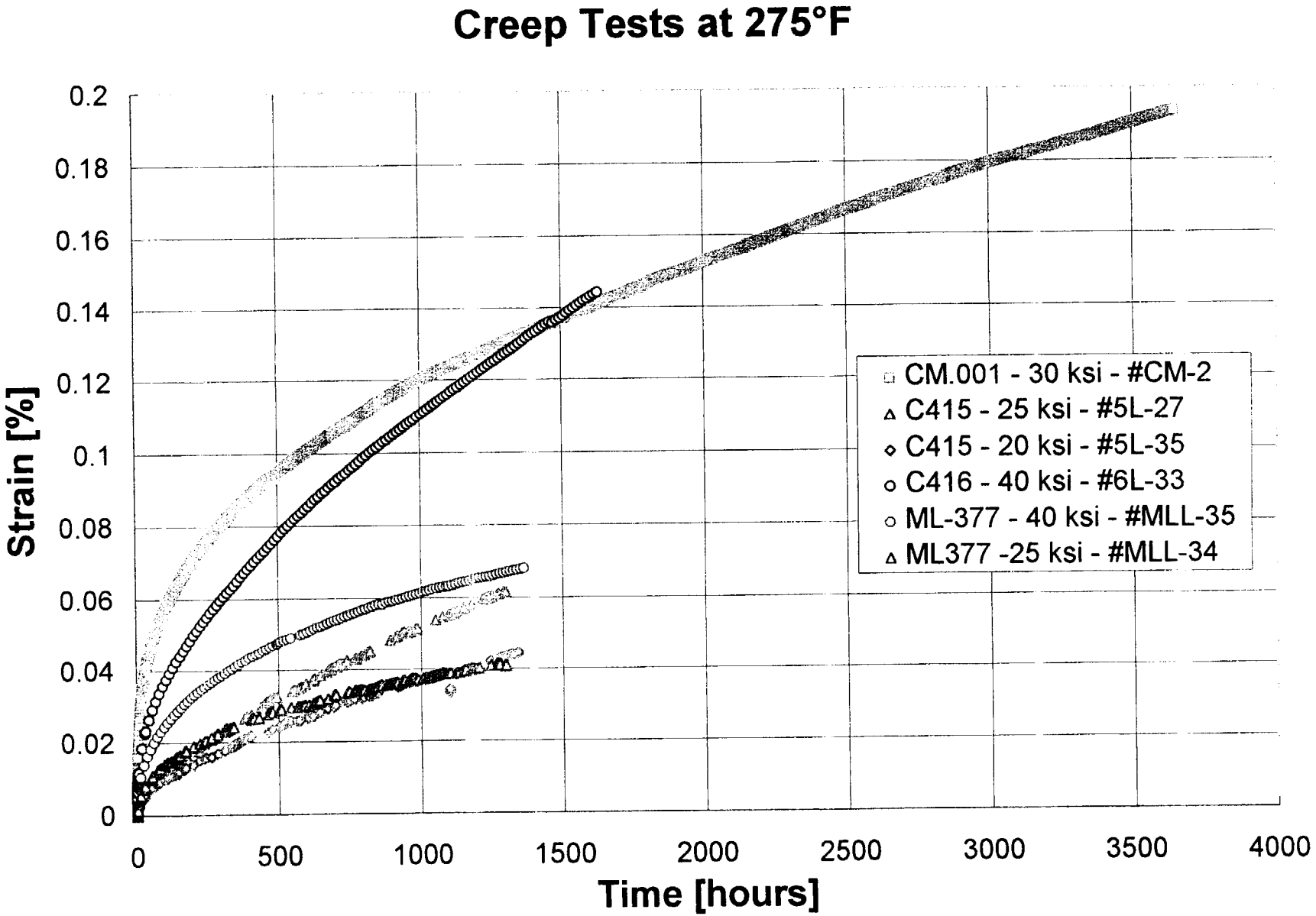
Creep Tests at 275°F
Strain [%]
0.2
0.18
0.16
0.14
0.12
0.1
0.08
0.06
0.04
0.02
0
0
500
1000
1500
2000
2500
3000
3500
4000
Time [hours]
CM.001 - 30 ksi - #CM-2
C415 - 25 ksi - #5L-27
C415 - 20 ksi - #5L-35
C416 - 40 ksi - #6L-33
ML-377 - 40 ksi - #MLL-35
ML377 -25 ksi - #MLL-34

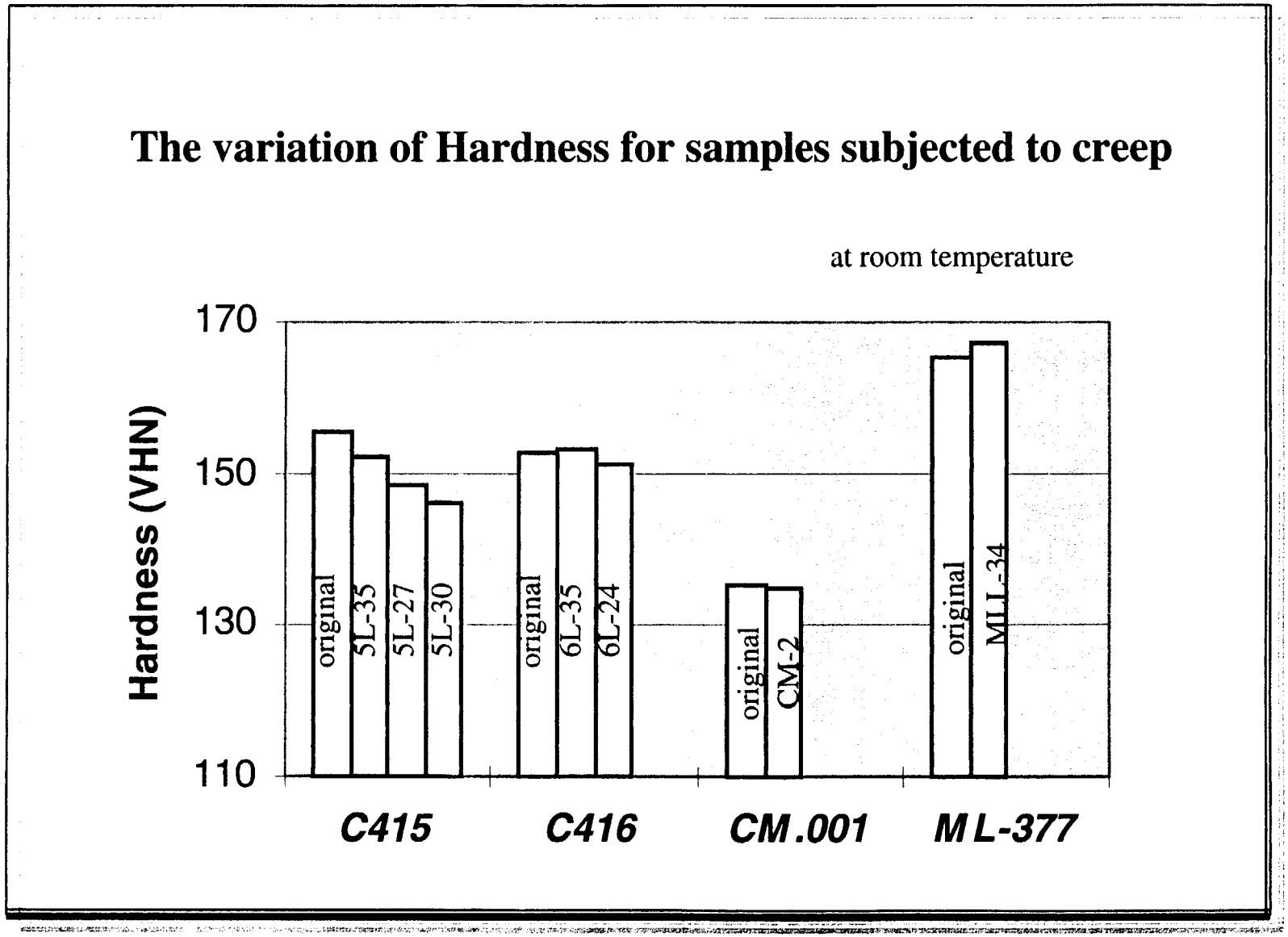
The variation of Hardness for samples subjected to creep
at room temperature
Hardness (VHN)
170
150
130
110
original
5L-35
5L-27
5L-30
original
6L-35
6L-24
original
CM-2
original
MLL-34
C415
C416
CM.001
ML-377

The variation of hardness for samples subjected to thermal exposure or creep

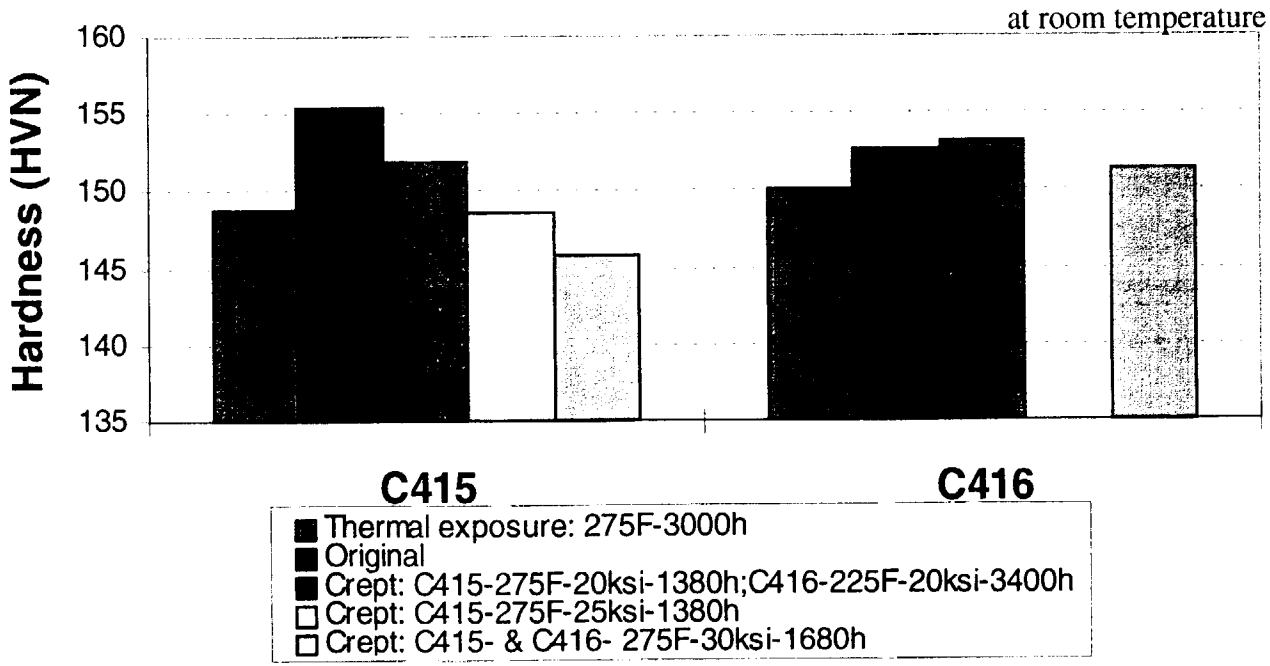

Selected Creep Tests at 275°F

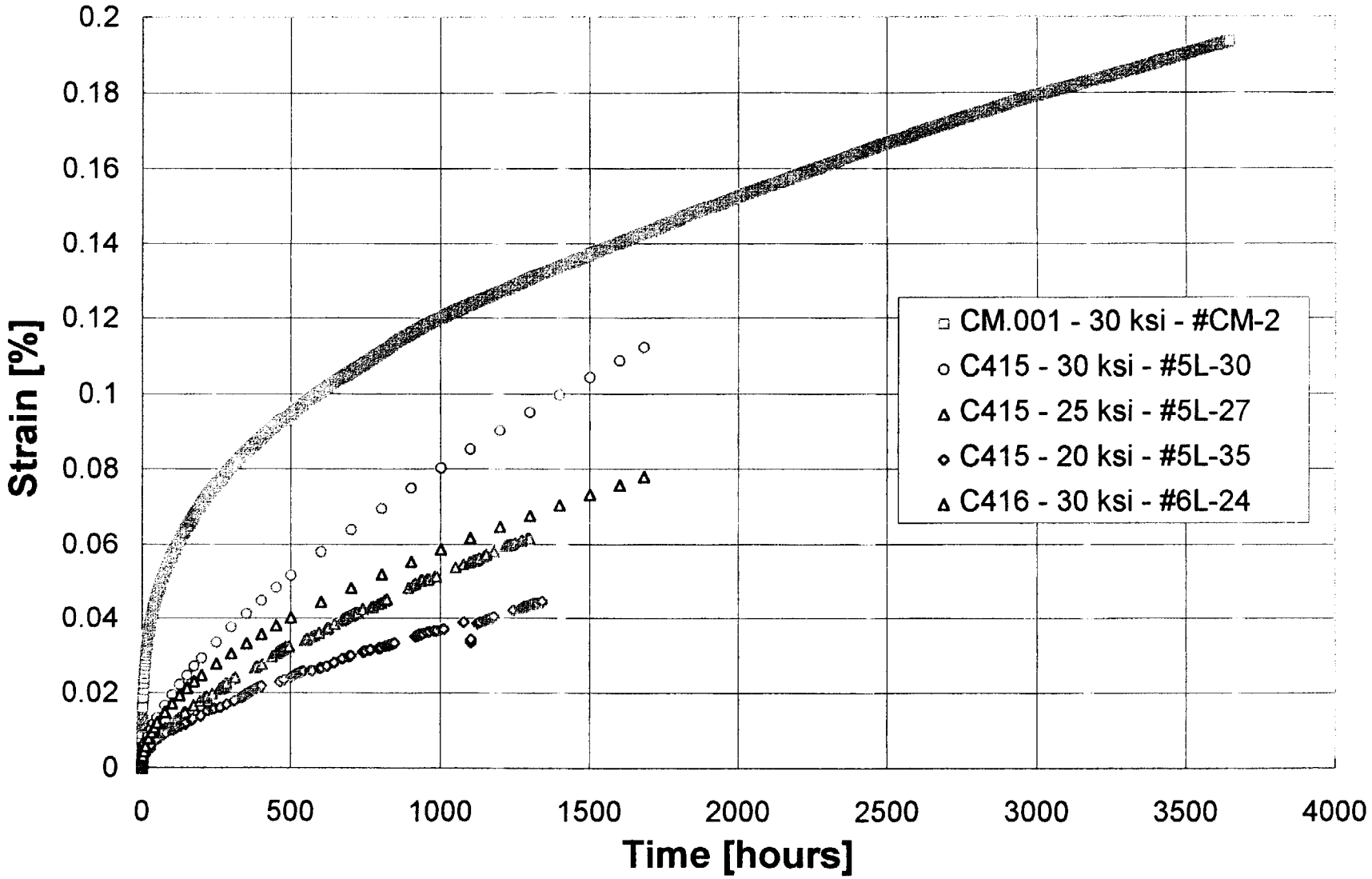

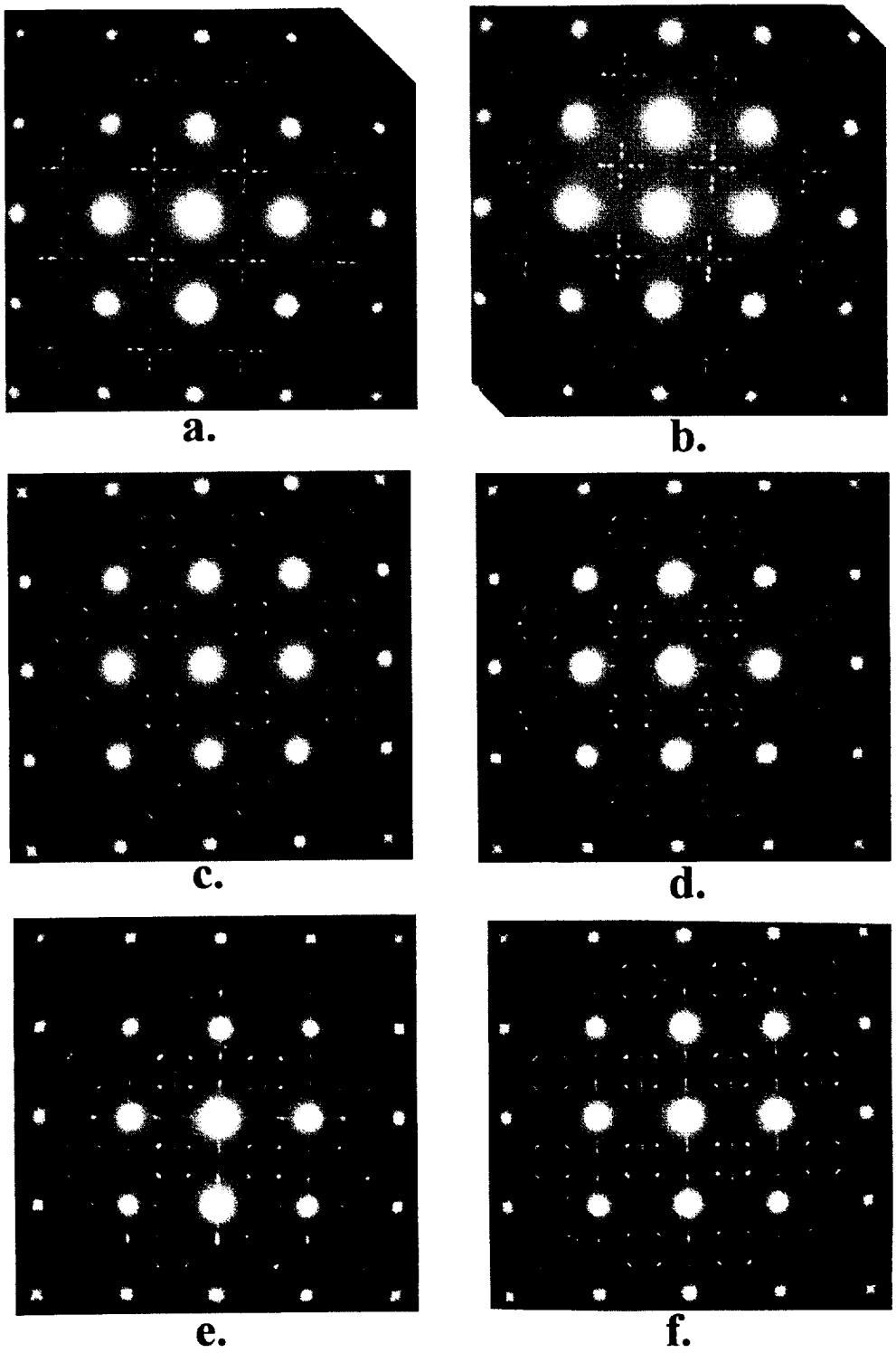

SAED patterns showing <001> zone axis from samples of:
a) CM.001 in T8; b) CM.001 in crept 275°F-30ksi-3647h;
c) C415 in T8; d) C415 in crept 275°F-30ksi-1681h;
e) C416 in T8; f) C416 in crept 275°F-30ksi-1681h.

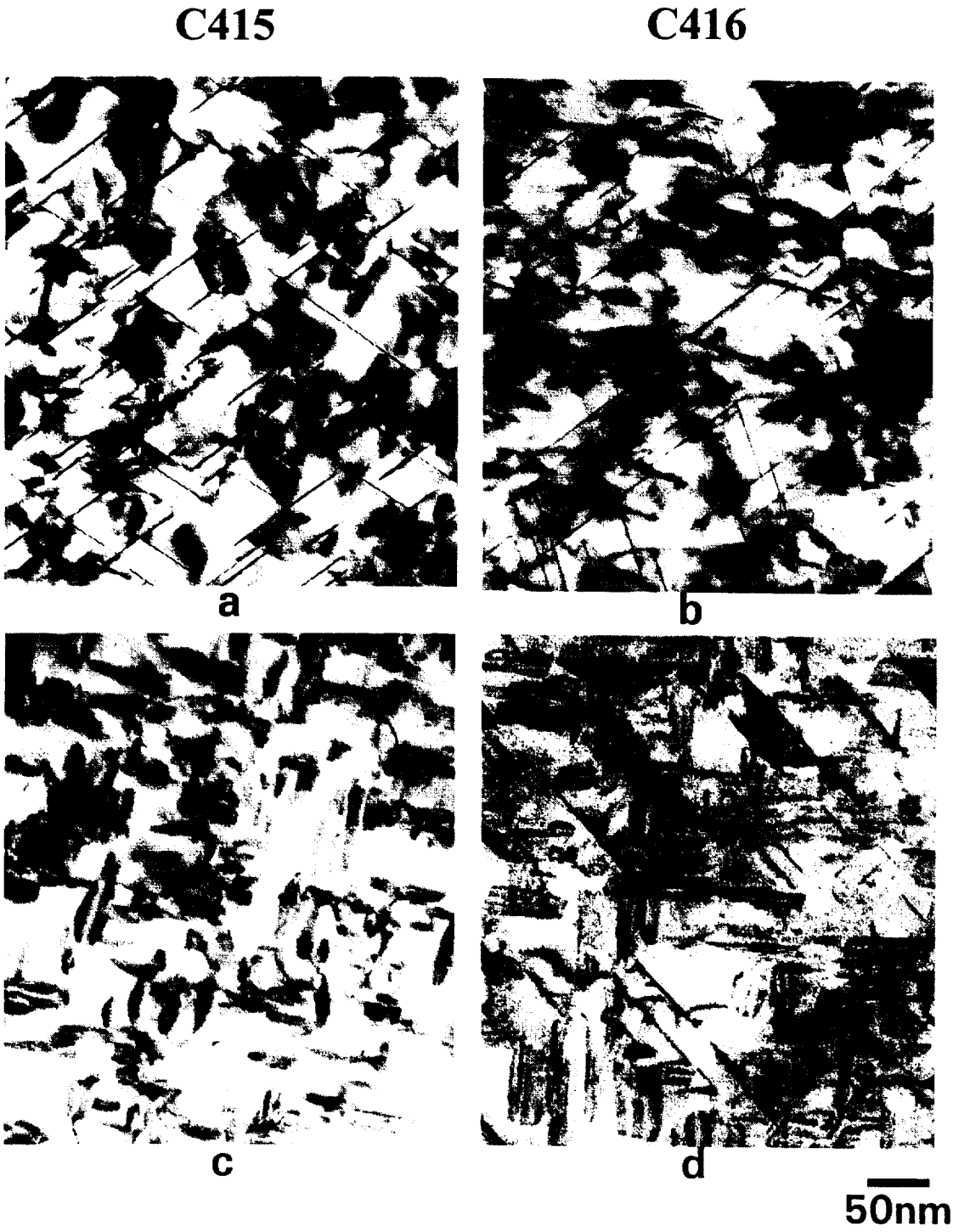

Bright-field electron micrographs of C415 and C416 in T8 condition.
a), b) the electron beam is approximately parallel to a <011>.
c), d) the electron beam is approximately parallel to a <001>.

C415

C416

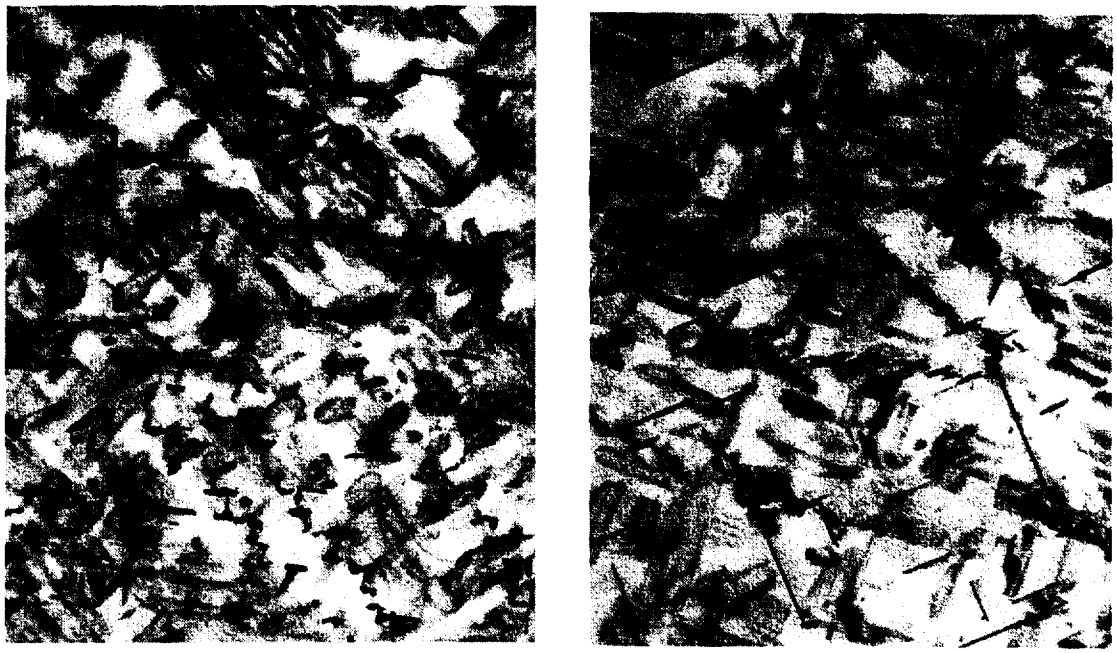

Bright-field electron micrographs of alloy C415 and C416 in the crept condition of 275°F-30ksi-1681h. The electron beam is approximately parallel to a <001> zone axis.

100nm

20nm

Transmission electron micrographs from C415 crept 1681h at 275°F-30ksi, showing S' precipitates on dislocations.

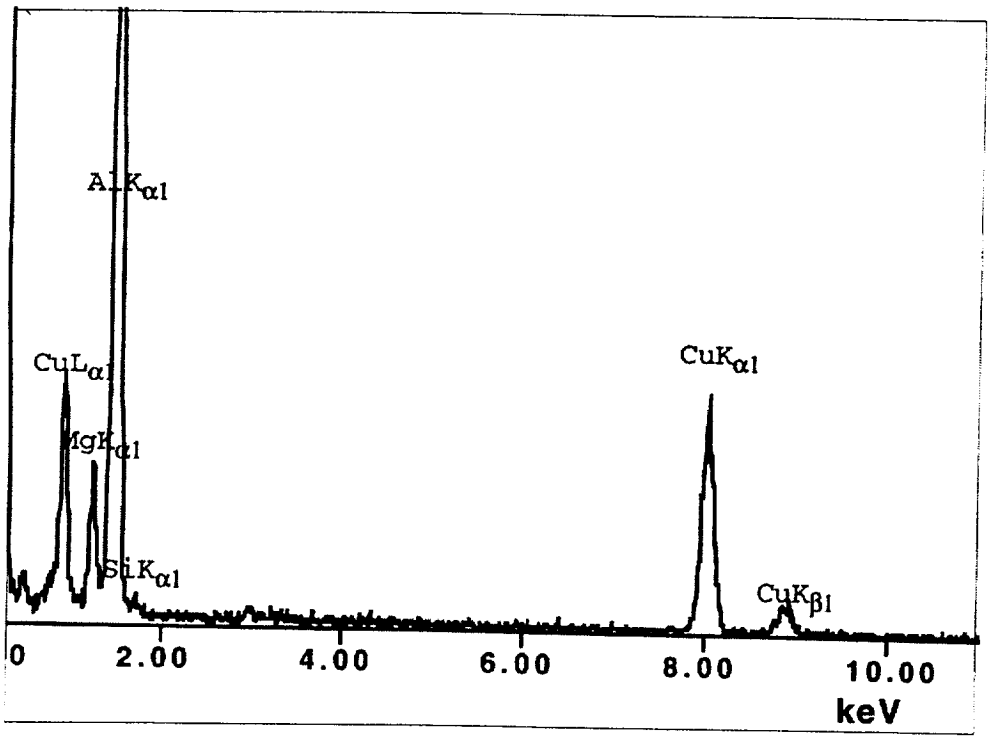

Energy dispersive X-ray spectrum recorded from the precipitates on dislocations.

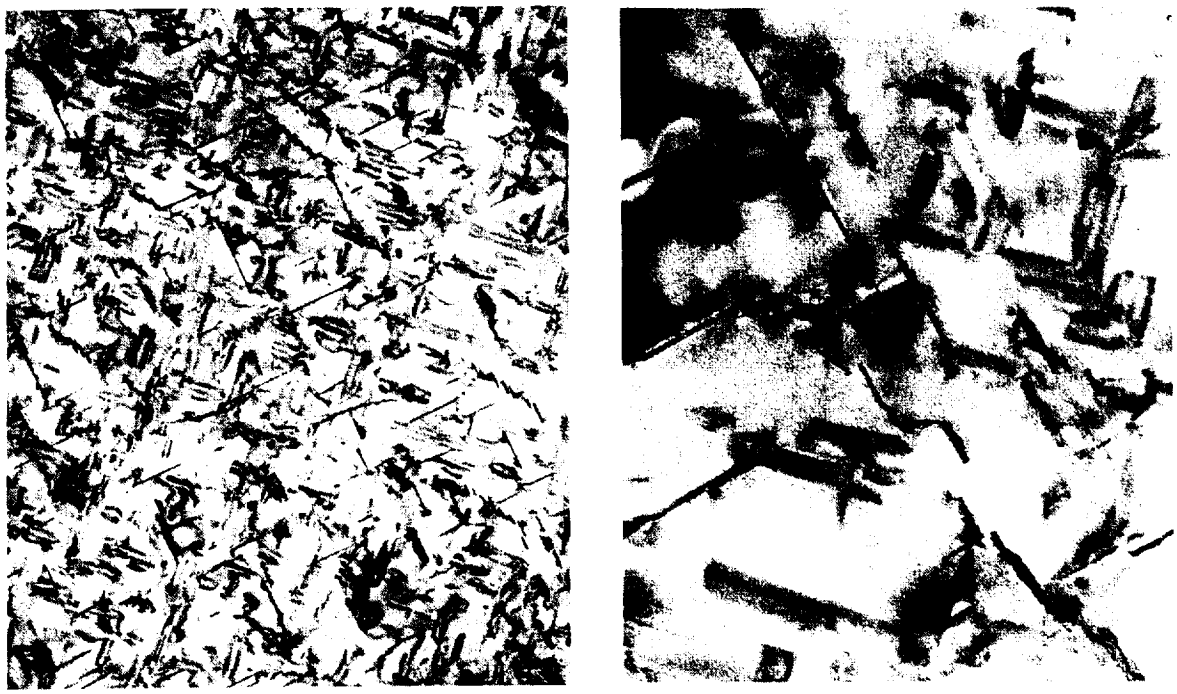

Transmission electron micrographs from C416 crept 1681h at 275°F-30ksi, showing theta prime precipitates on dislocations.

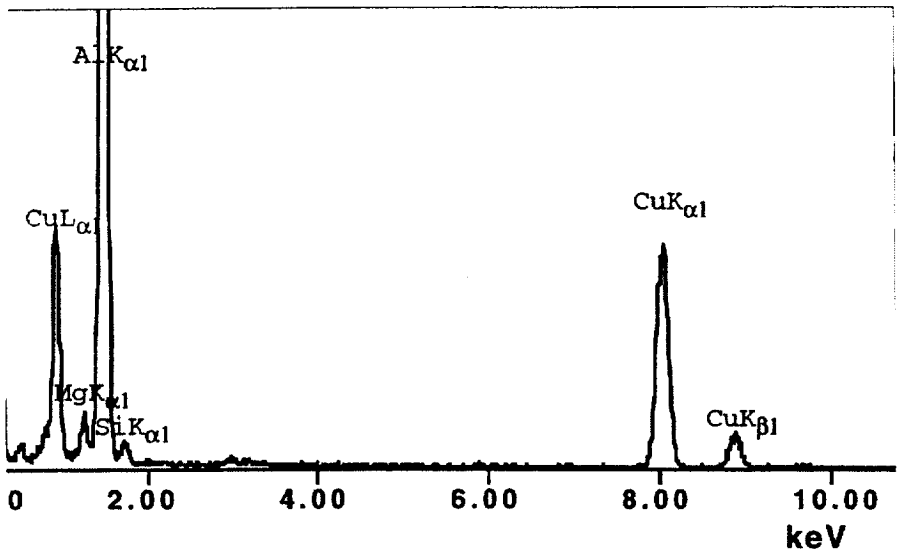

Energy dispersive X-ray spectrum recorded from the precipitates on dislocations.

a.
the operating reflection is {200}

50nm

b.

c.

Bright-field electron micrographs of C415 in the crept condition of :
a), b) 275°F-20ksi-1341h; c) 275°F-30ksi-1681h.
The electron beam is approximately parallel to <001>.

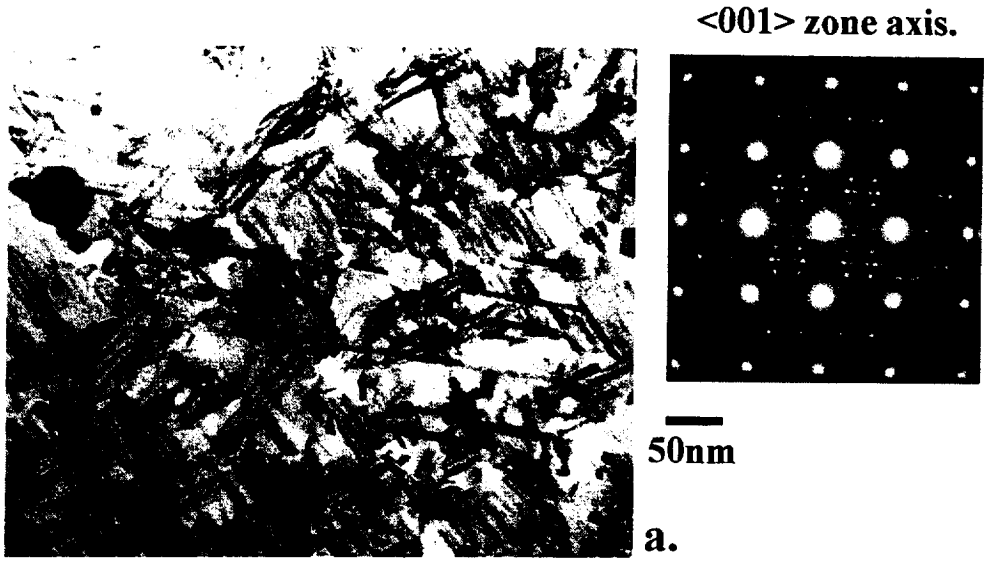

Bright-field electron micrographs from alloy C415 thermal exposed 3000 hours at 275°F.

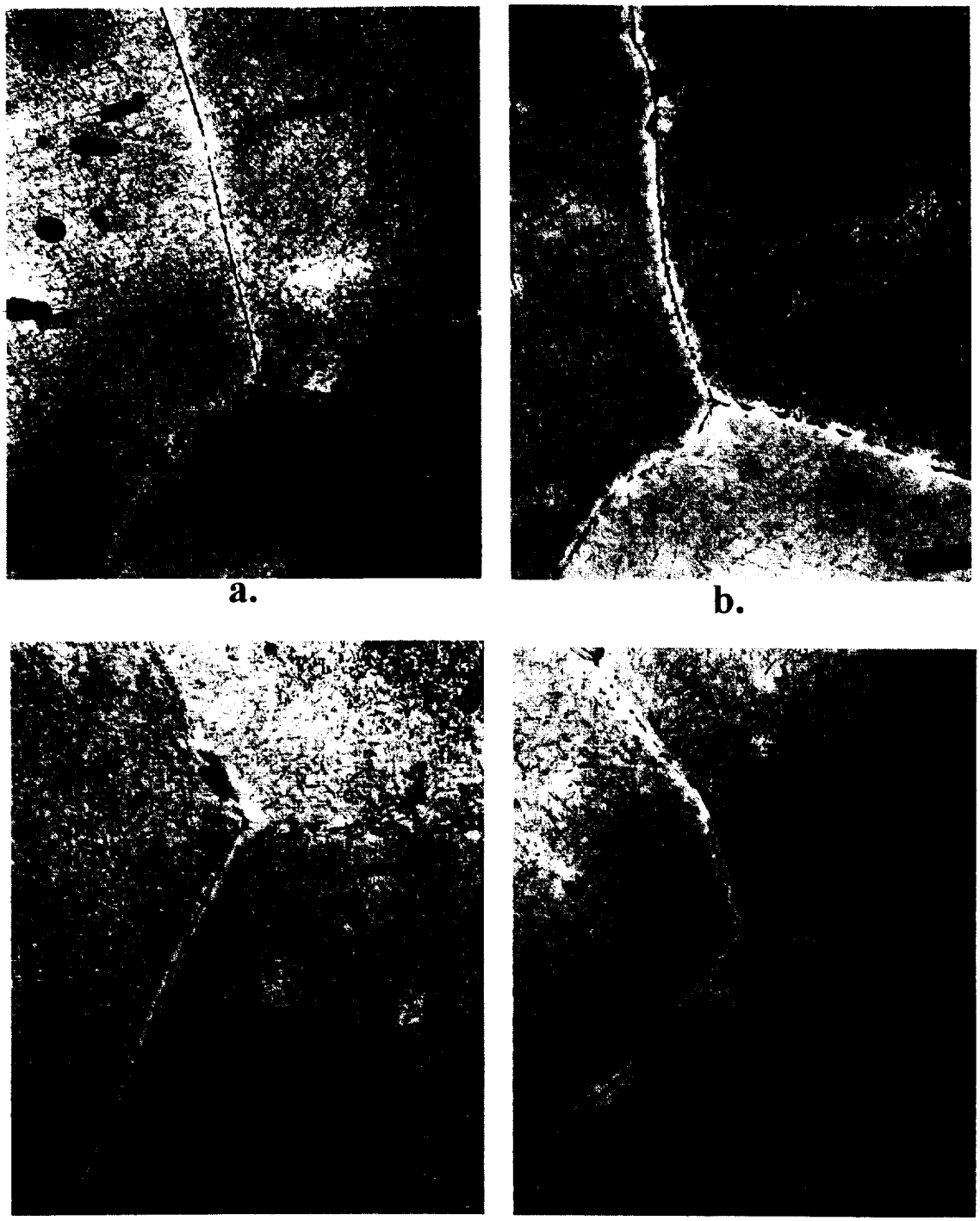

Transmission electron micrographs of alloy C415, showing the precipitates within the grain boundary region. a) prior to cree; b) thermal exposed 3000 hours at 275°F; c) crept 275°F-20ksi-1341h; d) crept 275°F-30ksi-1681h.

<001> zone axis.

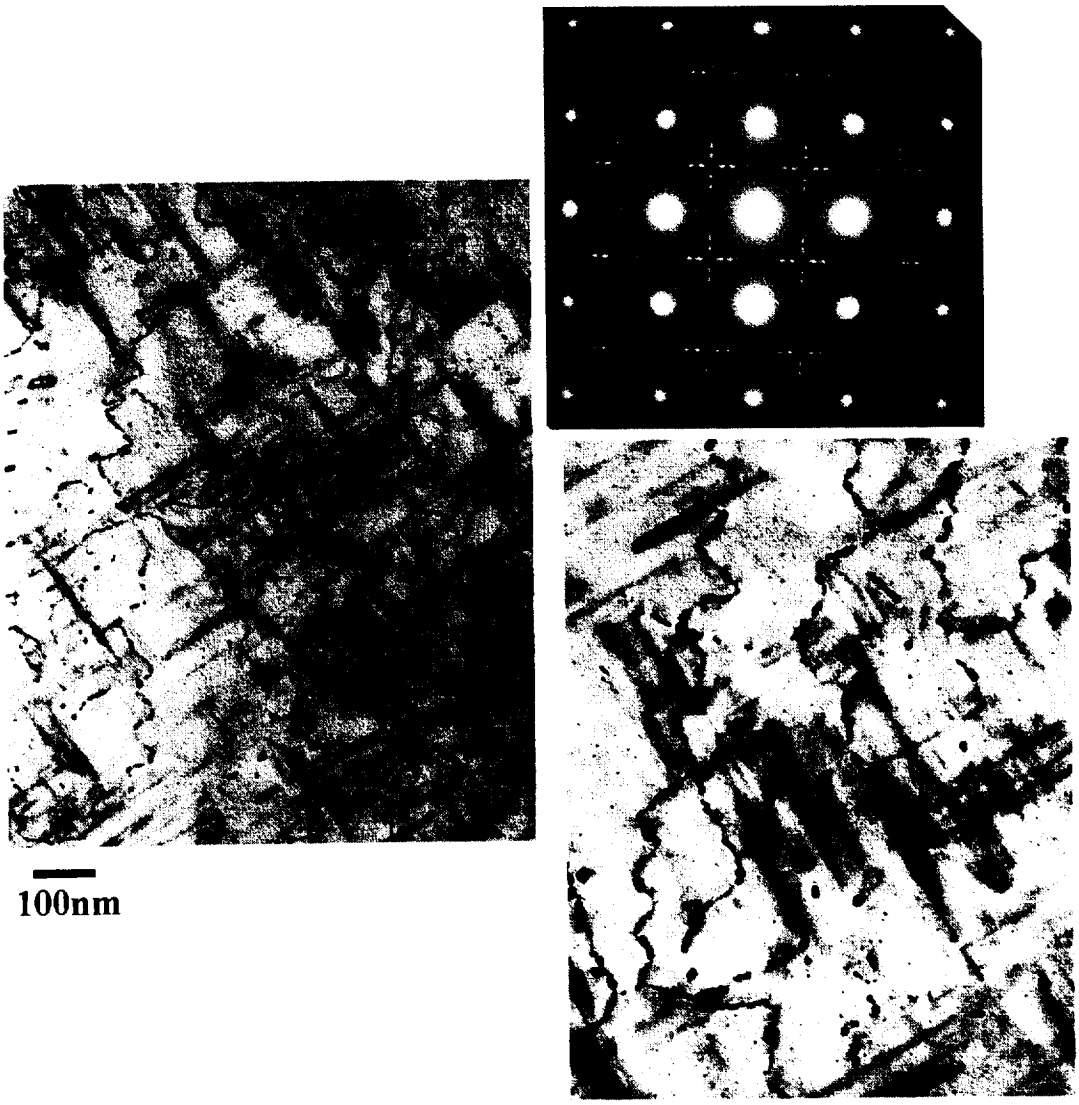

100nm

50nm

Bright-field electron micrographs from alloy CM.001 prior to creep.
The electron beam is approximately parallel to <001>.

<011> zone axis.

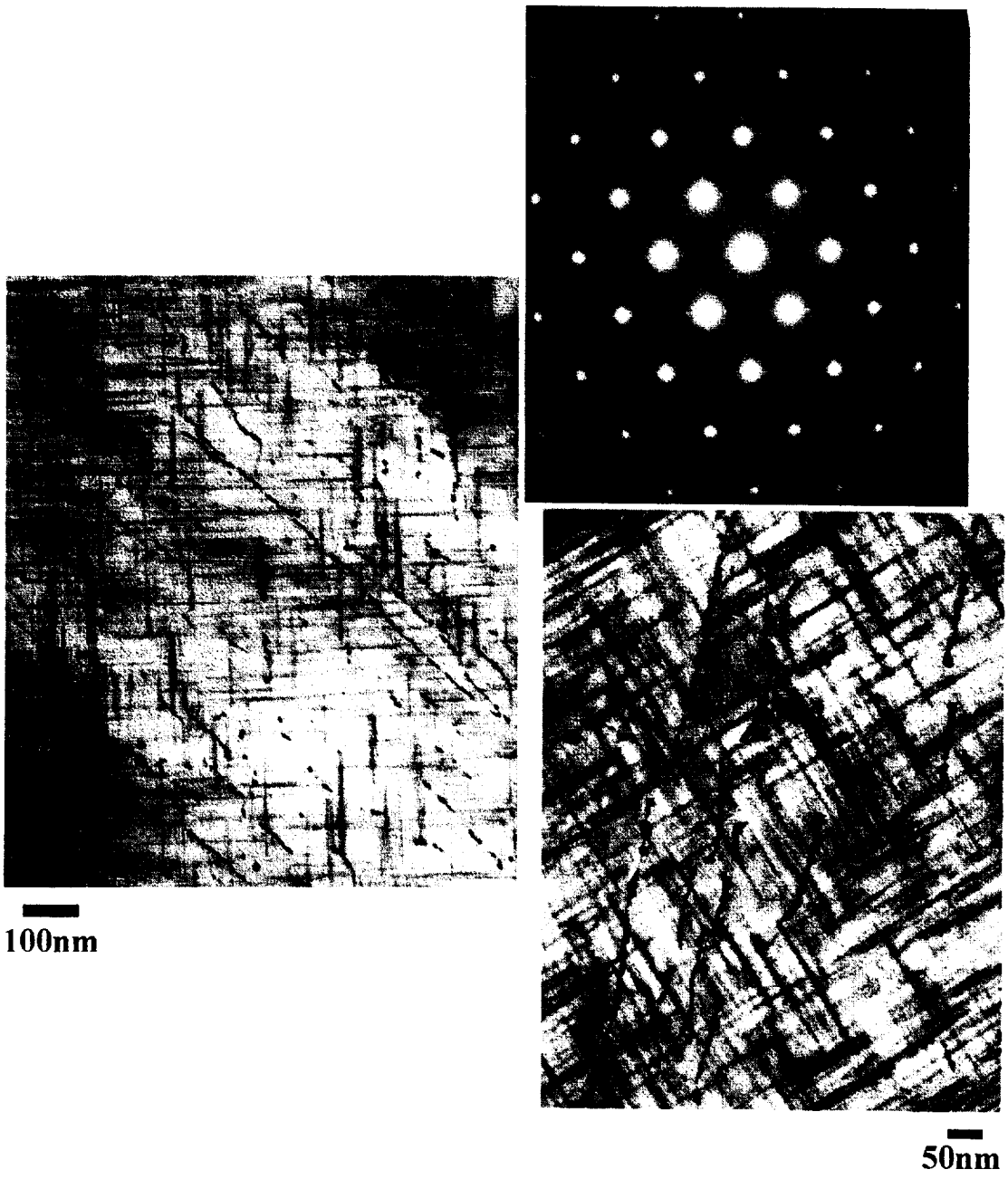

Bright-field electron micrographs from alloy CM.001 crept 3647 hours at 275°F-30ksi. The electron beam is approximately parallel to <011>.

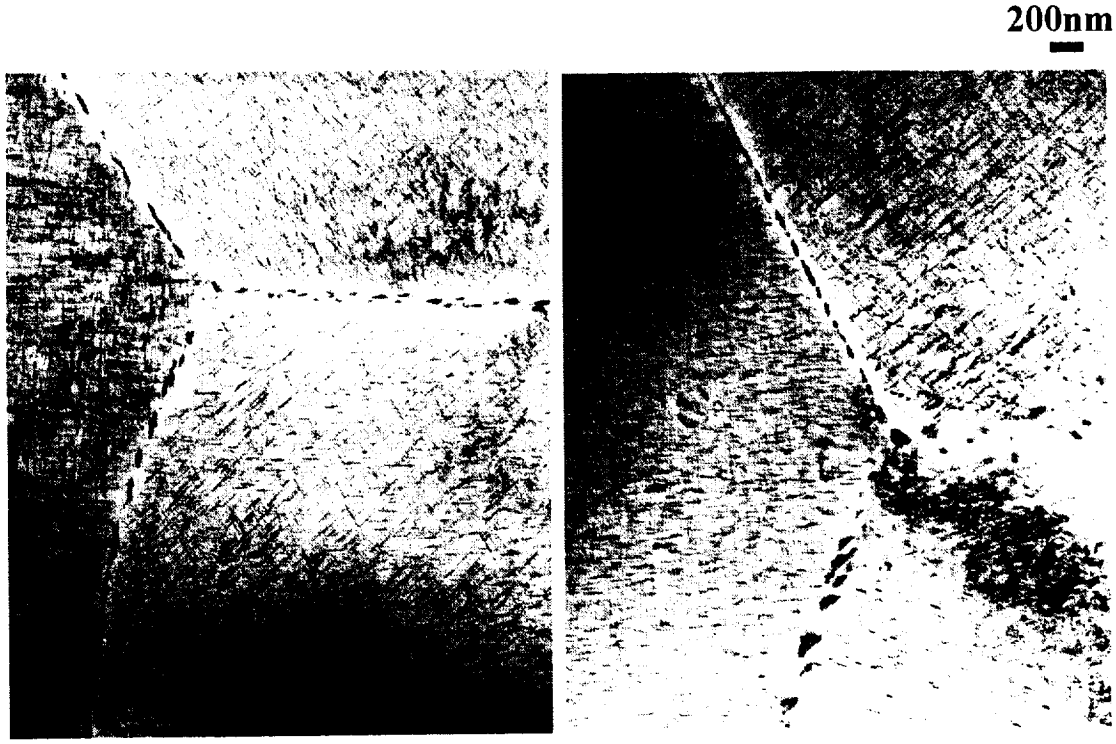

Transmission electron micrographs of alloy CM.001, showing precipitates within the grain boundary region. a) prior to creep; b) crept 275°F-30ksi-3647h.

Summary

- The creep curves generated provide a direct comparison of candidate alloys under service conditions.
- Creep behavior reflects microstructural and compositional influence.
- Creep resistance is enhanced by the Ω phase.
- S' precipitation at grain boundaries and dislocations contributes to the reduction in creep performance of C415 compared to C416.
- The annihilation of dislocations during S' precipitation reduces dislocation-induced hardening.
- Increased precipitation of S' at the expense of the other two strengthening phases may contribute to reduced creep resistance since S' is the least effective strengthener among Ω, θ' and S' precipitates.

DISTRIBUTION LIST

1-4	Mr. D.L. Dicus Contract Monitor Metallic Materials Branch, MS 188A NASA Langley Research Center Hampton, VA 23681-0001
5-6*	NASA Scientific and Technical Information Facility P.O. Box 8757 Baltimore/Washington International Airport Baltimore, MD 21240
7	Mr. Neil Price Grants Officer, M/S 126 NASA Langley Research Center Hampton, VA 23681-0001
8	Dr. Mark J. Shuart Materials Division, MS 188M NASA Langley Research Center Hampton, VA 23681-0001
9	Dr. Charles E. Harris Materials Division, MS 188M NASA Langley Research Center Hampton, VA 23681-0001
10	Mr. W. Barry Lisagor Metallic Materials Branch, MS 188A NASA Langley Research Center Hampton, VA 23681-0001
11	Dr. Robert S. Piascik Mechanics of Materials Branch NASA Langley Research Center Hampton, VA 23681-0001
12	Mr. W.D. Brewer Metallic Materials Branch, MS 188A NASA Langley Research Center Hampton, VA 23681-0001

13 Mr. Thomas T. Bales
Metallic Materials Branch, MS 188A
NASA Langley Research Center
Hampton, VA 23681-0001

14 Ms. Marcia S. Domack
Metallic Materials Branch, MS 188A
NASA Langley Research Center
Hampton, VA 23681-0001

15 Dr. Stephen J. Hales
Metallic Materials Branch, MS 188A
NASA Langley Research Center
Hampton, VA 23681-0001

16 Mr. R. Keith Bird
Metallic Materials Branch, MS 188A
NASA Langley Research Center
Hampton, VA 23681-0001

17 Mr. Eric K. Hoffman
Metallic Materials Branch, MS 188A
NASA Langley Research Center
Hampton, VA 23681-0001

18 Ms. Terryl A. Wallace
Metallic Materials Branch, MS 188A
NASA Langley Research Center
Hampton, VA 23681-0001

19 Ms. Joan G. Funk
HSR Project Office, MS 119
NASA Langley Research Center
Hampton, VA 23681-0001

20 Mr. Rodney H. Ricketts
HSR Project Office, MS 119
NASA Langley Research Center
Hampton, VA 23681-0001

21 Mr. Edward P. Phillips
Mechanics of Materials Branch, MS 188E
NASA Langley Research Center
Hampton, VA 23681-0001

22 Dr. Alex Cho
Reynolds Metals Co.
4th and Canal Street
Richmond, VA 23261

23 Mr. E.A. Colvin
Alcoa Technical Center
Route 780, 7th Street Road
Alcoa Center, PA 15069

24 Dr. Philip Hollinshead
Alloy Design Center
Alcoa Technical Center - C
100 Technical Drive
Alcoa Center, PA 15069-0001

25 Dr. Ravi Kahandal
McDonnell Douglas Aerospace
Mail Stop 36-90
3855 Lakewood Boulevard
Long Beach, CA 90846

26 Dr. William E. Quist
Boeing Commercial Airplane Group
MS 6H-CJ
P.O. Box 3707
Seattle, WA 98124-2207

27 Dr. John Papazian
Northrop Grumman Corporation
ATDC, A01-26
Bethpage, NY 11714-3581

28 Dr. Richard Lederich
McDonnell Douglas Aircraft Company
Mail Stop 111-1041
P.O. Box 516
St. Louis, MO 36166

29 Mr. David J. Chellman
Lockheed Martin Aeronautical Systems
Dept. 73-C1, Zone 0648
86 South Cobb Drive
Marietta, GA 30063-0648

30 Dr. Malcolm Ozelton
Manager, Metallic & Ceramic Materials
Northrop Corporation, B-2 Division
8900 E. Washington Boulevard
T241/GK
Pico Rivera, CA 90660-3737

31 Dr. James Staley
Alcoa Laboratories
Alcoa Technical Center
Route 780, 7th Street Road
Alcoa Center, PA 15069

32 Mr. Rodney R. Boyer
Boeing Commercial Airplane Group
MS 6H-CJ
P.O. Box 3707
Seattle, WA 98124-2207

33 Dr. Govind Chanani
Northrop Grumman Corporation
One Hornet Way, MC 9B70/W8
El Segundo, CA 90245

34 Dr. Michael T. Hahn
Northrop Grumman Corporation
T241/GK
8900 E. Washington Boulevard
Pico Rivera, CA 90660-3737

35 Professor Henry J. Rack
Clemson University
School of Materials, Chemical & Engineering
208 Rhode Hall
Clemson, SC 29634-0921

36 Dr. Pat Martin
Rockwell Science Center
1049 Camino Dos Rios
Thousand Oaks, CA 91360

37	Mr. John Fanning TIMET P.O. Box 2128 Henderson, NV 89009
38	M. Frederic Welter RMI Titanium Company P.O. Box 269 1000 Warren Avenue Niles, OH 44446-0269
39-40	E.A. Starke, Jr.; MS&E
41-42	R.P. Gangloff; MS&E
43	G.E. Stoner; MS&E
44	J.A. Wert; MS&E
45	J.R. Scully; MS&E
46	R.G. Kelly; MS&E
47	M. Rodeffer, Clark Hall
48	SEAS Preaward Research Administration
**	SEAS Postaward Research Administration

* One reproducible copy
** cover letter

Updated: April, 1997